Front propagation in weakly subcritical pattern-forming systems

Benjamin C. Ponedel, Hsien-Ching Kao, and Edgar Knobloch

Phys. Rev. E **96**, 032208 — Published 7 September 2017

DOI: 10.1103/PhysRevE.96.032208

Front propagation in weakly subcritical pattern-forming systems

Benjamin C. Ponedel,[1] Hsien-Ching Kao,[2] and Edgar Knobloch[1]

[1] *Department of Physics, University of California at Berkeley, Berkeley CA 94720, USA*
[2] *Wolfram Research, 100 Trade Center Dr., Champaign IL 61820, USA*

The speed and stability of fronts near a weakly subcritical steady state bifurcation are studied, focusing on the transition between pushed and pulled fronts in the bistable Ginzburg-Landau equation. Exact nonlinear front solutions are constructed and their stability properties investigated. In some cases the exact solutions are stable but are not selected from arbitrary small amplitude initial conditions. In other cases, the exact solution is unstable to modulational instabilities which select a distinct front. Chaotic front dynamics may result and is studied using numerical techniques.

I. INTRODUCTION

In this paper we are interested in the speed with which a nontrivial pattern invades either a stable homogeneous state or an unstable one. These types of problems arise frequently in applications [1–5] but the speed selection process remains imperfectly understood despite much effort. This is because in the former case the speed is inevitably selected by nonlinear processes (the pushed front case) while in the latter case selection may be via linear processes (the pulled front case) although nonlinear selection may survive well into the supercritical regime. Moreover, the selected speed depends in general on the initial condition, and in particular on the steepness of the front connecting the pattern to the homogeneous state at the initial instant.

In order to present a unified discussion of both processes we focus here on the bistable Ginzburg-Landau equation [6–13]

$$A_t = \mu A + A_{xx} + ia_1|A|^2A_x + ia_2A^2\bar{A}_x + d|A|^2A - |A|^4A. \tag{1}$$

This amplitude equation describes the evolution of the complex amplitude $A(x,t)$ on a slow spatial scale x and a slow time scale t in systems undergoing a weakly subcritical steady state bifurcation to a patterned state with wave number k_0 at $R = R_c$, where R is the bifurcation parameter. Thus the physical field of interest takes the form

$$u(x,t) = \epsilon A\left(\frac{x}{\epsilon^2}, \frac{t}{\epsilon^4}\right)e^{ik_0x} + \text{c.c.} + \text{h.o.t.}, \tag{2}$$

where ϵ is a small parameter measuring simultaneously the distance from the primary bifurcation at $R = R_c$ ($R = R_c + \epsilon^4\mu$) and the degree of subcriticality ($b = \epsilon^2 d > 0$). Thus $A \neq 0$ corresponds to a stripe pattern with wave number k_0 while $A = 0$ corresponds to the homogeneous state. Here b is the coefficient of the cubic term in the standard Ginzburg-Landau description of the primary bifurcation; its smallness requires a rescaling of the spatial and temporal scales, as indicated above, and leads to the appearance of the three new terms in Eq. (1), viz., the two terms with (real) coefficients a_1 and a_2, and of the quintic term whose coefficient has been scaled to -1 (stabilizing quintic term). It follows that either μ or d can be set equal to $+1$ by a suitable choice of ϵ. In the following we set $d = 1$ and use μ as the bifurcation parameter.

Equation (1) has the symmetries

$$A(x,t) \to \bar{A}(-x,t), \quad A(x,t) \to A(x,t)\,e^{i\phi}, \tag{3}$$

inherited from the assumed invariance of the original system for $u(x,t)$ under spatial reflections and translations with respect to the fast spatial scale. In the absence of spatial forcing on scales of order $O(\epsilon^{-2})$ the equation is also invariant under spatial translations with respect to the slow spatial scale x. The equation possesses a Maxwell-like point $\mu = \mu_M$ at which a multitude of stationary spatially localized structures of varying widths is present [12]. This point exists even when $a_2 \neq 0$, i.e., when the equation lacks gradient structure. In the latter case μ_M corresponds to the presence of a heteroclinic cycle connecting the trivial state $A = 0$ to a stationary nontrivial state $R_M e^{iq_M x}$ given by

$$R_M = \frac{12}{16 - (3a_1 - 5a_2)(a_1 + a_2)}, \tag{4}$$

$$q_M = \frac{3(a_1 + a_2)}{(3a_1 - 5a_2)(a_1 + a_2) - 16} \tag{5}$$

and back again.

Past studies of Eq. (1) focused mostly on the existence and stability of periodic solutions and coherent structures but a few also examine the well-posedness of the Cauchy problem. The existence and local stability of rotating wave solutions is treated in [8, 11–13] while nonlinear stability criteria are provided in [9]. The existence of pulses and fronts was examined in [8], and the persistence of front solutions when the coefficients acquire a small imaginary part was studied in [10]. In the case $a_2 = 0$ a free energy can be defined and it is known that the energy is bounded from below provided $|a_1| < \frac{4}{\sqrt{3}}$ [12]. This is a necessary condition for well-posedness of solutions of Eq. (1) when $a_2 = 0$. In the general case ($a_2 \neq 0$) the condition $|a_1 - a_2| < 2$ is known to be sufficient for global existence of solutions of the Cauchy problem [14]. The same condition is required for the global existence of periodic solutions of Eq. (1) and it was suggested though not proved that in this case the bound is

sharp [15]. However, the necessary and sufficient condition on the coefficients a_1, a_2 for the global existence of general solutions of Eq. (1) remains an open problem.

In the present work we are interested in the properties of traveling fronts that are present when $\mu \neq \mu_M$. Since the system is bistable two types of fronts are possible: pushed fronts describing the elimination of the nontrivial state by an invading trivial state ($\mu < \mu_M$) or vice versa ($\mu_M < \mu < 0$), and pulled fronts describing the invasion of a linearly unstable trivial state by a stable nontrivial state ($\mu > 0$). In fact, as first pointed out by van Saarloos [16] the transition between these two types of fronts does not take place exactly at $\mu = 0$, even when $a_1 = a_2 = 0$, and this transition is of particular interest in the present work as well.

The paper is organized as follows. In Sec. II we obtain a three-parameter family of exact traveling front solutions of Eq. (1) and study the stability of these solutions in the relevant parameter region. This solution set is a special case of that derived in [17]. The dynamic nature of these fronts is closely related to the stability of the asymptotic states at either end. In Sec. III we review the two basic regimes of front propagation distinguished by the stability properties of the background $A = 0$ state, and discuss the associated theoretical understanding of velocity selection in each case. Sections IV and V describe case studies of these two front propagation regimes, focusing in Sec. IV on the case in which $A = 0$ is stable and in Sec. V on the case in which it is unstable. In the latter case the "marginal stability criterion" of Dee and Langer [18] can then be applied to characterize the motion of the front, subject to certain restrictions on the initial conditions [19]. Section V also investigates the stability of the state deposited by the moving front with respect to spatial modulation. Brief conclusions follow in Sec. VI.

II. NONLINEAR FRONT

A procedure for finding exact coherent traveling structures of the Ginzburg-Landau equation has been outlined by van Saarloos and Hohenberg [20, 21]. Such traveling solutions inform bifurcation structure as well as dynamics and are thus of significant value. One of the most famous such examples is the one-parameter family of Nozaki-Bekki hole solutions for the complex Ginzburg-Landau equation which have been shown to play an important role in its dynamics [22]. In this section we derive an exact traveling front solution to Eq. (1) with fully general parameter dependence and study the region of existence and stability of the solution. These put restrictions on the parameter values for which the exact front is valid and dynamically relevant.

A. Spatial dynamics

If we restrict attention to traveling solutions, Eq. (1) can be rewritten in the form of three real first order ODEs [20] in a traveling frame with coordinate $\xi \equiv x - vt$. To do this we write

$$A(x,t) = W(\xi)e^{-i\omega t}, \tag{6}$$

where ω is a constant, and $W(\xi) \equiv a(\xi)e^{i\phi(\xi)}$. In addition, we introduce the quantities $q \equiv \phi'$ and $\kappa \equiv \frac{a'}{a}$, where the prime denotes differentiation with respect to ξ. This procedure yields the real-valued equations

$$a' = a\kappa, \tag{7}$$

$$q' = -(a_1 + a_2)\, a^2\kappa - q(v + 2\kappa) - \omega, \tag{8}$$

$$\kappa' = a^2\left[(a_1 - a_2)\, q - 1\right] + a^4 - \mu + q^2 - v\kappa - \kappa^2. \tag{9}$$

The traveling front solutions that we seek correspond to heteroclinic orbits between fixed points $(a, q, \kappa) = (a_N, q_N, 0)$ (the nontrivial state) and $(0, q_L, \kappa_L)$ (the trivial state). Given arbitrary values of the parameters μ, a_1, a_2, these heteroclinics may exist only for certain values of v, ω. If a heteroclinic orbit exists only for discrete values of v and ω (for each set of μ, a_1, a_2) it will be known as a "discrete front" and otherwise it is a "k-parameter front" where k indicates the number of free parameters.

We suppose, without loss of generality, that the front solution approaches $(a_N, q_N, 0)$ as $\xi \to -\infty$ (the source or upstream state) and $(0, q_L, \kappa_L)$ as $\xi \to \infty$ (the sink or downstream state). It follows that the former must be unstable in the space variable ξ while the latter must have at least one stable eigendirection. An upper bound on the number of free parameters within a family of such heteroclinic solutions is therefore determined by the dimensions of the unstable manifold of the source fixed point and the stable manifold of the sink [21]. If the source has n unstable eigendirections then the solution curve must lie in the corresponding n-dimensional unstable manifold. This condition restricts the number of degrees of freedom of the solution curve by 1 leaving $n-1$ degrees of freedom. Adding the two free parameters v, ω the total number of degrees of freedom becomes $n + 1$. A necessary condition for the existence of a heteroclinic between the source and sink is that the solution curve also lies in the stable manifold of the sink. If the sink has l unstable eigendirections this requirement generically requires that l variables are fixed thereby leaving $k \equiv n - l + 1$ variables free. If $k > 0$ the solution curve corresponds to a k-parameter front, if $k = 0$ it is a discrete front, and if $k < 0$ no heteroclinic orbit exists between the two fixed points. A complete analysis of the fixed points and associated stable/unstable manifold dimensions of Eqs. (7)–(9) is carried out in [8].

We follow [20] in using the Ansatz

$$q = q_N + e_0\left(a^2 - a_N^2\right), \quad \kappa = e_1\left(a^2 - a_N^2\right), \tag{10}$$

and suppose that the resulting front travels with speed $v = v_N$. This front is a discrete front, i.e., $k = 0$, and both ω and v are determined by the system parameters. Differentiating the Ansatz and using Eq. (7) we find that $q' = 2e_0a^2\kappa$ and $\kappa' = 2e_1a^2\kappa$. Next, we eliminate q and κ from Eqs. (8) and (9), obtaining a pair of polynomial identities in a. In order for these to be satisfied identically each coefficient of the polynomials must vanish. These conditions produce a set of algebraic equations sufficient to determine the constants $a_N, q_N, e_0, e_1, v_N, \omega_N$. There are generically two sets of values of the constants that solve these equations due to a fold bifurcation in the $\mu < 0$ region. The explicit form of the front can be found by recalling the definition of κ and solving the second relation in Eq. (10) as a first order differential equation for a:

$$W(\xi) \equiv a_N e^{iq_N\xi}\left(1 + e^{2a_N^2 e_1 \xi}\right)^{-\frac{1}{2} - i\frac{e_0}{2e_1}}. \qquad (11)$$

Here $e_1 > 0$ since we choose fronts that decay to zero as $\xi \to \infty$. Figure 1 shows a sample plot of the solution (11) with $(a_1, a_2) = (2, 3)$ and $\mu = 0$. The front solution connects the rotating wave state $A = a_N e^{i(q_N\xi - \omega_N t)}$ as $\xi \to -\infty$ to the trivial state $A = 0$ as $\xi \to \infty$.

We now exhibit the explicit Ansatz parameters for $(a_1, a_2) \neq (0, 0)$. For simplicity of presentation we first introduce the auxiliary parameters

$$\begin{aligned}
\Gamma &= 16 - (3a_1 - 5a_2)(a_1 + a_2), \\
\Delta &= 16 - (a_1 + a_2)\left[4a_1 - 3a_2^3 - a_1a_2^2 + 2\left(a_1^2 - 10\right)a_2\right], \\
\Upsilon &= 8 - (3a_1 - 7a_2)(a_1 + a_2), \\
\Lambda &= 2 + a_2(a_1 + a_2), \qquad (12)
\end{aligned}$$

yielding $e_0 = -\frac{1}{4}(a_1 + a_2)$, $e_1 = \frac{1}{4}\sqrt{\frac{\Gamma}{3}}$, $\omega_N = -q_N v_N$, together with

$$\begin{aligned}
a_{N\pm}^2 &= \frac{2(5\Lambda - 6) \pm 2\Upsilon\sqrt{(2\Lambda + \mu\Delta)/\Gamma}}{\Delta}, \\
q_{N\pm} &= \frac{a_1 + a_2}{\Delta}\left[-2\Lambda \pm (6 - \Lambda)\sqrt{(2\Lambda + \mu\Delta)/\Gamma}\right], \qquad (13) \\
v_{N\pm} &= \sqrt{\frac{\Gamma}{3}}\frac{\Lambda - 6 \pm \sqrt{(2\Lambda + \mu\Delta)\Gamma}}{\Delta}.
\end{aligned}$$

One of these solutions $(\pm)$ is stationary at the Maxwell-like point $\mu = \mu_M(a_1, a_2) \equiv -\frac{3}{\Gamma}$ [12]. Depending on the sign of the quantity $\Lambda - 6$ the stationary front may be located on either the a_{N+} or the a_{N-} branch. These branches meet at a fold at $2\Lambda + \mu\Delta = 0$. In addition, since $\omega_N + q_N v_N = 0$, the source state is always stationary in the original frame. The coefficients for the Ansatz shown here may be obtained from the more general solution derived in [17] that uses this Ansatz in a quintic Ginzburg-Landau equation with complex coefficients.

The Ansatz yields well-defined solutions even when $\Delta = 0$, despite the vanishing denominators in Eq. (13), although there is now only one solution rather than two

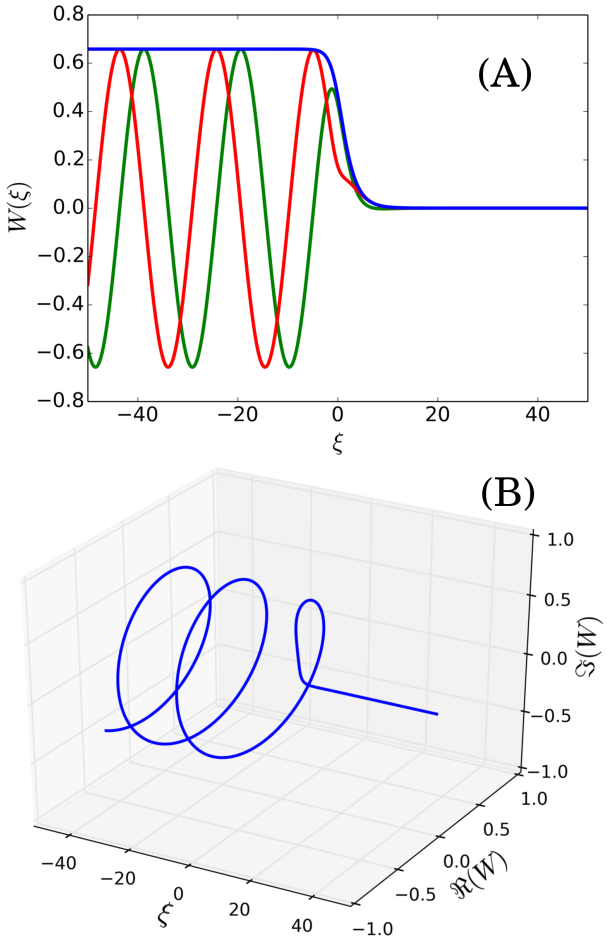

FIG. 1. The nonlinear front with parameters $(a_1, a_2) = (2, 3)$ and $\mu = 0$ shown at a fixed time. (a) The real (green) and imaginary (red) parts of the solution $A(\xi, \cdot)$ along with its amplitude $|A|$ in blue. (b) A 3D representation of the solution in (a).

(up to an overall sign):

$$\begin{aligned}
a_N^2 &= \frac{\mu\Upsilon^2 - 9(a_1 + a_2)^2}{(6 - 5\Lambda)\Gamma}, \\
q_N &= \frac{a_1 + a_2}{4\Lambda\Gamma}\left[\mu(6 - \Lambda)^2 - 6\Lambda\right], \qquad (14) \\
v_N &= \frac{\Gamma^{\frac{1}{2}}(\mu\Gamma + 3)}{2\sqrt{3}(6 - \Lambda)}.
\end{aligned}$$

Here e_0 and e_1 are as above but all the auxiliary variables are understood to be restricted to the curve $\Delta = 0$. There is now only one branch of fronts with positive a_N and no fold in the branch. The Maxwell point is still given by $-\frac{3}{\Gamma}$. This case is not discussed in [17].

In the special case $a_1 = a_2 = 0$ we recover the result of [16, 23]. The front solution (11) then takes the form

$$W(\xi) \equiv \frac{a_N}{\sqrt{1 + e^{2a_N^2\xi/\sqrt{3}}}} \qquad (15)$$

with

$$a_N^4 - a_N^2 - \mu = 0, \qquad v_N = \frac{4a_N^2 - 3}{\sqrt{3}}, \tag{16}$$

provided $\mu > -\frac{1}{4}$. The polynomial equation of a_N^2 in Eq. (16) has two real roots. A front with $a_N^2 = \frac{1+\sqrt{1+4\mu}}{2}$ connects a stable constant amplitude state to the stable trivial state and travels with speed $v_N = \frac{2\sqrt{1+4\mu}-1}{\sqrt{3}}$. Such a front moves in the positive ξ direction when $\mu > -\frac{3}{16}$ and in the negative ξ direction when $-\frac{1}{4} < \mu < -\frac{3}{16}$. The Maxwell point is at $\mu_M = -\frac{3}{16}$. The other solution, which only exists when $-\frac{1}{4} < \mu < 0$, always travels in the negative ξ direction as it connects an unstable constant amplitude state to the stable trivial state.

In fact, the general case (13) reduces to Eq. (16) along the whole line $a_1 = -a_2$, along which all of the constants Γ, Δ, Υ, Λ become independent of *both* a_1 and a_2. This reduction results because in this case the cubic terms in Eq. (1), $\left[d|A|^2 + ia_1(\bar{A}A_x - A\bar{A}_x)\right]A$, can be written in the special form $(d - 2a_1q)|A|^2A$ with $q = 0$. As a result the coefficient a_1 drops out.

For strongly nonlinear front propagation problems it is useful to develop a characterization of the intrinsic length scale in the model. In view of the exact front solution (11), it is natural to define this length scale, hereafter λ, as the inverse spatial decay rate of the front envelope, i.e., $\lambda \equiv \frac{1}{e_1 a_N^2}$. We show this length scale, evaluated at the Maxwell point $\mu = \mu_M(a_1, a_2)$, in Fig. 2. The figure shows that in the case of a_{N+}, increasing $|a_1|$ leads to front steepening while increasing $|a_2|$ leads to broadening. Unsurprisingly, the a_{N-} solution has both a smaller amplitude and a smaller spatial decay rate than its sibling above the fold. Specifically, when $a_2 > 0$ the a_{N-} front steepens for decreasing a_1 and broadens for increasing a_2 throughout the bulk of the parameter regime.

B. Existence conditions for the nonlinear front

The Ansatz (10) does not always generate a front solution. For this to be the case the coefficients in Eq. (13) must be real and the amplitude of the nontrivial asymptotic state must be positive, i.e.,

$$\Gamma > 0, \qquad a_N^2 > 0, \qquad 2\Lambda + \mu\Delta > 0. \tag{17}$$

These conditions place restrictions on the allowed values of a_1, a_2 and μ. We remark that $\Gamma > 0$ implies $\Lambda > 0$, a result that follows from the identity $\Gamma = 8\Lambda - 3(a_1 + a_2)^2$. Verifying these conditions requires an understanding of the allowed values of μ which we examine next.

The front solutions typically bifurcate from the trivial state in a subcritical pitchfork bifurcation, leading to the coexistence of the trivial state with the two front solutions, $a = a_{N\pm}$. This bifurcation is located at $\mu = \mu_P \equiv \frac{9(a_1+a_2)^2}{\Upsilon^2} \geq 0$ and the initial front amplitude scales as $a_N \propto |\mu - \mu_P|^{\frac{1}{2}}$ unless $5\Lambda = 6$ in which case $a_N \propto |\mu - \mu_P|^{\frac{1}{4}}$ and the pitchfork is degenerate. As a consequence, when $\Delta(5\Lambda - 6) > 0$ a fold bifurcation is present at $\mu = \mu_F \equiv -\frac{2\Lambda}{\Delta}$. This fold lies to the left (right) of the pitchfork bifurcation when the pitchfork is subcritical (supercritical) and no fronts of the assumed form is present $\mu < \mu_F$ ($\mu > \mu_F$), with only one front present for $\mu > \mu_P$ ($\mu < \mu_P$). Note that $\mu_P = 0$ along the line $a_1 = -a_2$.

The imposition of the requirements (17) leaves distinct generic parameter regimes within which the nonlinear front (11) exists. These depend on the values of Δ, Υ, and Λ. The first of these that we shall consider depends on the signs of Δ and $5\Lambda - 6$. Most of the parameter space is covered by $\Delta > 0$ but there is a sliver near the boundary of the existence region where $\Delta < 0$ (Fig. 3). While the former case displays expected behavior, the latter complicates the validity of the Ansatz and in many cases only one of the solutions in Eqs. (13) remains valid. In the following analysis we shall consider the effects of passing through the sign change in the auxiliary variables by increasing a_1. Since $5\Lambda > 6$ whenever $\Delta > 0$ there are three possible regimes encountered as a_1 increases from 0: (1) $\Delta > 0$ and $5\Lambda > 6$, (2) $\Delta < 0$ and $5\Lambda > 6$, and (3) $\Delta < 0$ and $5\Lambda < 6$. As a_1 increases from 0, Δ decreases towards zero and $\mu_F \to -\infty$. When $\Delta = 0$ there is no fold bifurcation on the front branch: the branch of exact fronts bifurcates from the trivial state at $\mu = \mu_P$ and extends to $\mu = -\infty$. This behavior persists into the region $\Delta < 0$ and $5\Lambda > 6$ in which only the a_{N+} solution is valid. Finally, if $|a_2| > \frac{1}{\sqrt{5}}$ then a third regime becomes accessible in which $\Delta < 0$ and $5\Lambda < 6$. At $5\Lambda = 6$ the pitchfork switches from subcritical to supercritical and in so doing regenerates a fold at μ_F, now to the right of the pitchfork. For $\mu_P \leq \mu \leq \mu_F$ both solutions of Eqs. (13) are valid.

The remaining degenerate parameter regimes involve Υ and Λ (Fig. 3), and have direct physical interpretation as a result of their effect on the μ dependence of the solutions. First, as $\Upsilon \to 0$ from both above and below $\mu_P \to \infty$. When $\Upsilon = 0$, Δ is always positive and $5\Lambda > 6$ so both solutions in Eqs. (13) are valid but have the same μ-independent amplitude, $a_N^2 = \frac{2(5\Lambda-6)}{\Delta}$. A similar phenomenon occurs in the case $\Lambda = 6$ when the deposited wave number, q_N, becomes independent of μ and takes the same value for both solutions in Eqs. (13). That is, the nonlinear front leaves the same patterned state in its wake regardless of the forcing μ. Because μ represents the bifurcation parameter that pushes the system into the pattern-forming regime, a dependence of a_N and q_N on μ is to be expected. The fact that this expectation fails in these subcases is indicative of a nontrivial front selection mechanism and a nongeneric balance among the cubic nonlinear terms of Eq. (1). These effects are new and cannot be seen in the well-studied case $a_1 = a_2 = 0$.

Bifurcation diagrams for the amplitude of the front solutions for sample parameters are shown in Figs. 4 and 5 in which we plot $\|W\|_\infty = a_N$ versus the parameter μ.

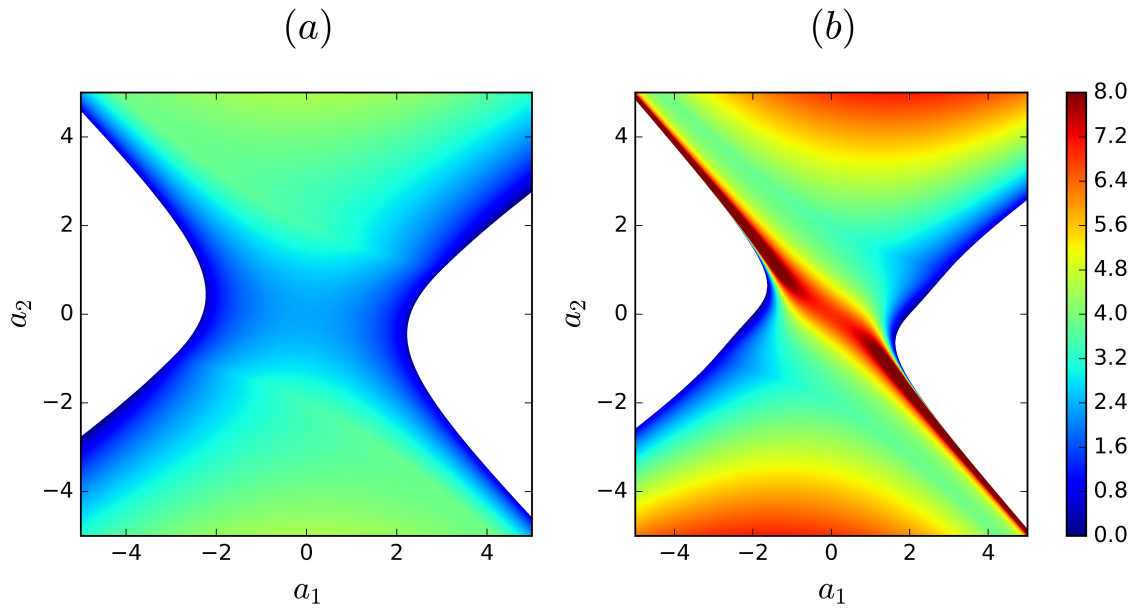

FIG. 2. The length scale $\lambda \equiv \left(e_1 a_N^2\right)^{-1}$ at the Maxwell point $\mu = \mu_M(a_1, a_2)$ for fronts on (a) the a_{N+} branch and (b) the a_{N-} branch. Regions colored dark red represent values ≥ 8. The solution that lies below the fold on the branch of front solutions has a smaller amplitude and decay rate as compared to that above the fold.

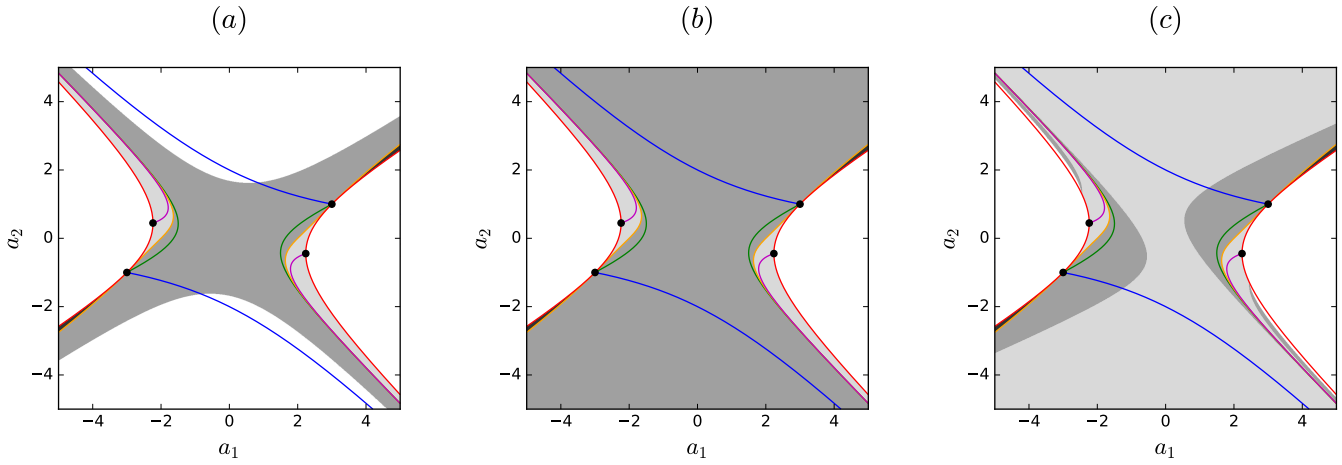

FIG. 3. The existence regions for $a_{N\pm}$ when (a) $\mu = -0.1$, (b) $\mu = 0$, (c) $\mu = 0.1$. The dark grey indicates existence of both solutions, light grey indicates existence of only a_{N+}, black indicates existence of only a_{N-}, while white implies nonexistence of both solutions. The lines $\Gamma = 0$ (red), $\Lambda = 6$ (blue), $5\Lambda = 6$ (magenta), $\Upsilon = 0$ (green) and $\Delta = 0$ (orange) are shown restricted to the region $\Gamma > 0$, required for the validity of the Ansatz (10). The dots indicate the locations $(a_1, a_2) = (\pm 3, \pm 1)$, $\left(\pm\sqrt{5}, \mp\frac{1}{\sqrt{5}}\right)$ on the curve $\Gamma = 0$.

First, Fig. 4(a) demonstrates the generic behavior of the nonlinear fronts for $a_2 = 0$, while Figs. 4(b) and (c) show nongeneric behavior that arises when the remaining key coefficients Υ and Δ pass through zero. Since $\Upsilon = 0$ at $a_1 = \sqrt{\frac{8}{3}}$ while $\Delta = 0$ at $a_1 = 2$ we separate Fig. 4 into three diagrams around $a_1 = 0$, $\sqrt{\frac{8}{3}}$, and 2. In the bulk of the parameter space the generic case with $a_1, a_2 \neq 0$ shares the same qualitative characteristics as the cases in Fig. 4 with the corresponding signs of Δ, Υ and Λ. Second, Fig. 5 focuses on the regime $5\Lambda - 6 \approx 0$, only realizable for $|a_2| > \frac{1}{\sqrt{5}}$. Here the pitchfork bifurcation responsible for the branch of fronts switches from subcritical to supercritical (at $5\Lambda = 6$). The resulting solution branch moves towards the left with decreasing a_1 until the Ansatz fails at $a_1 = -\frac{7}{3} \approx -2.33$ where $\Gamma = 0$.

C. Stability of exact front solutions

We analyze the linear stability of a front by linearizing Eq. (1) about such a front, i.e., writing $A = W(\xi)e^{-i\omega t}(1 + \delta(\xi, t))$, $|\delta| \ll 1$. This yields

$$\delta_t = \delta_{\xi\xi} + U\delta_\xi + ia_2|W|^2\bar{\delta}_\xi + V(\delta + \bar{\delta}), \tag{18}$$

where

$$\begin{aligned} U(\xi) &\equiv v + 2W^{-1}W_\xi + ia_1|W|^2, \\ V(\xi) &\equiv |W|^2 - 2|W|^4 + i\left(a_1\bar{W}W_\xi + a_2W\bar{W}_\xi\right). \end{aligned} \tag{19}$$

The quantities $U(\xi) \equiv U_r + iU_i$ and $V(\xi) \equiv V_r + iV_i$ may be computed from the identities

$$\begin{aligned} |W|^2 &= \frac{a_N^2}{1 + e^{2a_N^2 e_1 \xi}}, \\ W^{-1}W_\xi &= iq_N + (e_1 + ie_0)\left(|W|^2 - a_N^2\right). \end{aligned} \tag{20}$$

We search for temporal eigensolutions of the form $\delta(\xi, t) = e^{\sigma t}(\delta_1 + \delta_2) + e^{\bar{\sigma} t}(\bar{\delta}_1 - \bar{\delta}_2)$, where δ_1 and δ_2 are functions of ξ alone, leading to the eigenvalue problem

$$\sigma \begin{pmatrix} \delta_1 \\ \delta_2 \end{pmatrix} = \begin{pmatrix} \partial_{\xi\xi} + U_r\partial_\xi + 2V_r & i\left(U_i - a_2|W|^2\right)\partial_\xi \\ i\left(U_i + a_2|W|^2\right)\partial_\xi + 2V_i & \partial_{\xi\xi} + U_r\partial_\xi \end{pmatrix} \begin{pmatrix} \delta_1 \\ \delta_2 \end{pmatrix} \equiv \mathcal{L} \begin{pmatrix} \delta_1 \\ \delta_2 \end{pmatrix}. \tag{21}$$

The spectrum of the operator $\mathcal{L}$ consists of a point spectrum σ_p and the essential spectrum σ_c. However, this operator is non-normal: it does not commute with its adjoint. Non-normal operators do not obey the spectral theorem, may not have orthogonal eigenfunctions and can have a point spectrum with high sensitivity to perturbations [24, 25]. Such operators arise, for example, in the study of spatially varying fluid flows [25, 26]. Conclusions about stability from point spectra of non-normal operators are complicated by the possibility of transient growth and we opt in this work to treat only the essential spectrum of $\mathcal{L}$, which can be computed analytically.

The essential spectrum for a front solution consists of the union of the essential spectra of the $\xi \to \pm\infty$ states. The trivial state (at $\xi \to \infty$) is only stable when μ is negative. In the notation of [13] infinitesimal perturbations of the periodic state present at $\xi \to -\infty$ have the growth rate

$$\sigma(q) = ivq - (g + q^2) \pm \sqrt{g^2 + q^2(2g - f)}, \tag{22}$$

where q is the perturbation wave number and

$$g \equiv 2(\mu - q_N^2) + \left[1 + q_N(a_2 - a_1)\right]a_N^2, \tag{23}$$

$$f \equiv (4 + a_2^2 - a_1^2)a_N^4 - 2\left[1 + q_N(a_2 + a_1)\right]a_N^2 - 4q_N^2. \tag{24}$$

We call a solution linearly stable if its spectrum is contained in the left half of the complex plane. In [13] it was shown that this rotating wave state is stable if and only if f and g are both nonnegative. Thus the essential spectrum of the front is stable provided $f, g \geq 0$ and $\mu < 0$. It was further shown in [13] that there are two distinct regimes by which the rotating wave can go unstable: (I) $f < 0$ and $f \leq g$ or (II) $g < 0$ and $f > g$. The first is characterized by a marginal wave vector with nonzero real part and the latter by one with zero real part. Though a complete analysis of the point spectrum is not included here we can calculate the eigenfunctions of the zero eigenvalue analytically. This eigenvalue has double multiplicity: translation symmetry gives rise to a zero eigenvalue "Goldstone mode" [27] $\delta(\xi, t) = W^{-1}W_\xi$ while rotation symmetry generates the zero eigenvalue phase mode $\delta(\xi, t) = i$.

Although the rotating wave states of (1) form a one parameter family of states (for fixed system parameters) [12, 13], the front solution computed here selects one particular rotating wave in the asymptotic limit $\xi \to -\infty$. This reduction enables us to plot the stability in the (a_1, a_2) plane for fixed μ. In Figs. 6 and 7 we exclude the spectrum of $A = 0$ and plot the stability of the rotating wave selected by the nonlinear front Ansatz in the two qualitatively distinct regimes $\mu \lessgtr 0$. For $\mu < 0$ the a_{N+} branch is stable in a region of parameter space

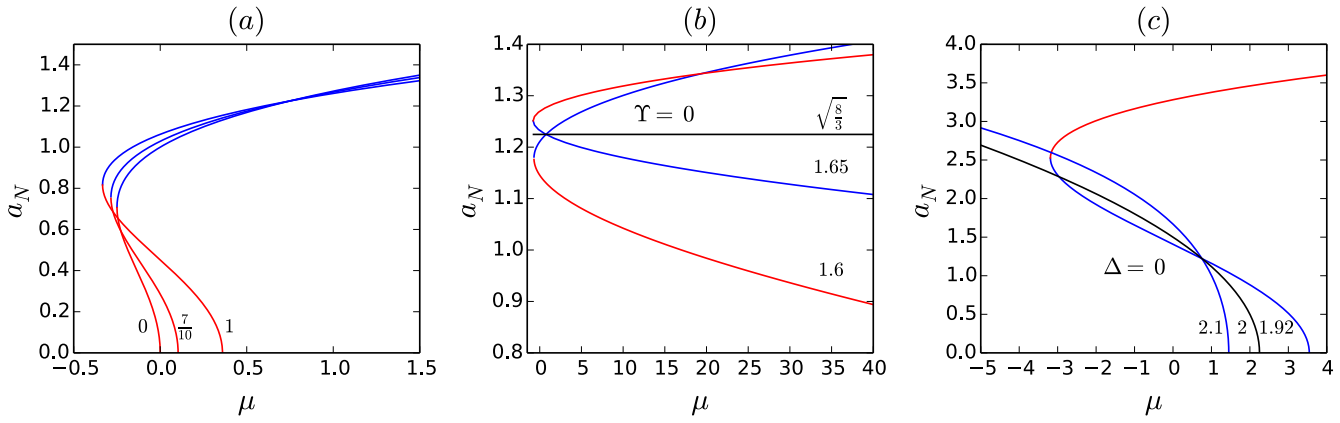

FIG. 4. The front amplitudes a_{N+} (blue) and a_{N-} (red) for (a) $\Upsilon > 0$, $\Delta > 0$, (b) several values of $\Upsilon \approx 0$ while $\Delta > 0$, and (c) for several values of $\Delta \approx 0$ while $\Upsilon < 0$. The parameter values in each of these plots are $a_2 = 0$ and (a) $a_1 = (0, 0.7, 1)$, (b) $a_1 = \left(1.6, \sqrt{\frac{8}{3}}, 1.65\right)$, and (c) $a_1 = (1.92, 2, 2.1)$ as indicated in the panels. The special cases $\Upsilon = 0$ and $\Delta = 0$ are shown in black.

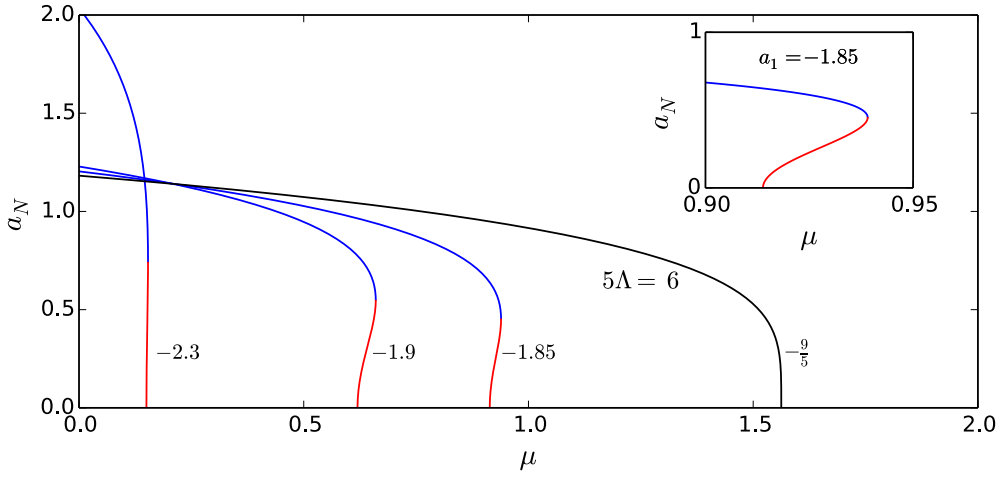

FIG. 5. The front amplitudes a_{N+} (blue) and a_{N-} (red) as functions of μ for $a_2 = 1$ and $a_1 = -2.3, -1.9, -1.85, -\frac{9}{5}$; the latter branch, corresponding to $5\Lambda = 6$, is shown in black.

surrounding the line $a_1 = -a_2$, while the a_{N-} branch is rarely stable. For $\mu > 0$ the a_{N+} branch is stable in a significantly larger parameter region while the a_{N-} branch remains mostly unstable. Despite the large regions of instability revealed in the figure, the dynamical significance of an unstable rotating wave in the wake the front solution is more subtle. Because we are concerned with the asymptotic dynamics of the front as $t \to \infty$, instabilities behind it are only relevant provided that they propagate to the right with a speed not less than that of the front, i.e., to have an effect the instability must be absolute in the frame of the leading edge. The propagation speeds of these instabilities and their effect on the front are computed and analyzed in Sec. V B below.

The stability of the deposited rotating wave is particularly relevant at the Maxwell point $\mu = -\frac{3}{\Gamma}$ at which the front is stationary. This front is associated with the branch a_{N+} when $\Lambda - 6 < 0$ and a_{N-} when $\Lambda - 6 > 0$. We show the stability of the rotating wave selected by the stationary front in Fig. 8. It is easy to see from the figure that the region of stability is contained in the intersection of $\Gamma(a_1, a_2) > 0$ and $\Lambda(a_1, a_2) < 6$, so the rotating wave selected at the Maxwell point is only stable for fronts on the a_{N+} branch. The instability of the a_{N-} fronts is always of type II and has been confirmed using direct numerical simulation. The stability at $\mu = \mu_M$ of other branch of the Ansatz for which $v_N \neq 0$ can also be studied. The rotating wave selected by this branch is always unstable. When $\Lambda - 6 < 0$ the instability can be either of type I or II depending on parameters but for $\Lambda - 6 > 0$ it is always of type II.

III. FRONT DYNAMICS

We now turn to the question: "at what speed does a front between the patterned state and the trivial state propagate?", a phenomenon known as "spreading." It turns out that in many cases physically relevant initial conditions evolve into a front whose profile and "spreading" speed as $t \to \infty$ depend only on the system parameters and not on the initial data. Indeed, in many systems these asymptotic front speeds are unique for a large class of sufficiently localized initial conditions [28, 29].

Front propagation into a trivial state may arise in one of two qualitatively different ways. When $\mu < 0$ and the primary pattern-forming instability is subcritical, as assumed here, the system exhibits bistability between a stable trivial state and a stable nontrivial state, implying that the heteroclinic orbit between them corresponds to a front propagating into a stable state. This type of front is known as a "pushed" front. In systems with gradient structure (here $a_2 = 0$) the speed of such fronts is determined by the energy difference between the two stable states connected by the front. Propagation favors the state with lowest energy and the front velocity vanishes when the energy difference vanishes, i.e., at the Maxwell point. More generally ($a_2 \neq 0$), a stationary front of the Ansatz (10) corresponds to a Maxwell-like point and the front speed v in the vicinity of this point satisfies $v \approx v_M \equiv \frac{3(\mu-\mu_M)}{2(-\mu_M)^{\frac{3}{2}}} \left[4 - a_2(a_1 + a_2)\right]^{-1}$ [13]. In contrast to this picture, when $\mu > 0$ the trivial state is unstable and the speed of the resulting "pulled" front is frequently (but not always) determined by the properties of the linearization of Eq. (1) about $A = 0$. This change in the speed selection mechanism is a consequence of the growth of infinitesimal perturbations of the $A = 0$ state ahead of the front [18].

Problems of front propagation into unstable states have been known in the plasma physics community since the 1950s [30] but the term "marginal stability" was not proposed until 1983 by Dee and Langer [18]. The marginal stability conjecture is based on the idea that the front propagating into an unstable state that is selected at large times is marginally stable in the comoving frame. In practical terms this means that in the comoving frame of the selected front instabilities of the unstable state ahead of the front are neither advected to $\xi = -\infty$ behind the front nor grow into a faster front. This description is closely related to the notions of convective and absolute instability in systems with imposed flow. A system is said to be *convectively* unstable if sufficiently spatially localized perturbations grow but do not spread upstream rapidly enough to overcome the imposed flow. It is called *absolutely* unstable if the perturbation can spread upstream against the flow. In the former case the perturbation at any fixed position ultimately decays, while in the latter case instability is ultimately observed at all locations in the domain. The marginal stability condition corresponds to the transition between convective and absolute instabilities in the comoving frame.

When the state $A = 0$ ahead of the front is unstable, growth of small amplitude perturbations ahead of the leading edge is governed by the linearization of the PDE around $A = 0$. We assume that the front speed is determined by the growth of these perturbations as described by the marginal stability conjecture. According to this conjecture the spreading speed can be computed from the linear evolution equation $A_t = \mathcal{L}A$ via the dispersion relation for linear waves of the form $A = A_0 e^{\sigma(q)t + iqx}$, where $q = q_r + iq_i$. Consider a compactly supported initial perturbation of the system and express the solution in terms of its Fourier decomposition $A(x,t) = \int_{\mathbb{R}} \hat{A}(q) e^{\sigma(q)t + iqx} dq$. By shifting into the frame of the right edge of this perturbation and applying a saddle-point analysis in the limit $t \to \infty$ one finds that the group speed must vanish. Moreover, the perturbation must be neutrally stable in this frame. These requirements are summarized by the conditions [4]

$$\Re\left[\sigma'(q)\right] = 0, \quad -\Im\left[\sigma'(q)\right] = \frac{\Re[\sigma(q)]}{\Im[q]} = v^*, \quad \Im[q] > 0 \tag{25}$$

from which one may compute the *complex*-valued wave number q^* and the linear spreading speed $v^* = \frac{\Re[\sigma(q^*)]}{\Im[q^*]}$

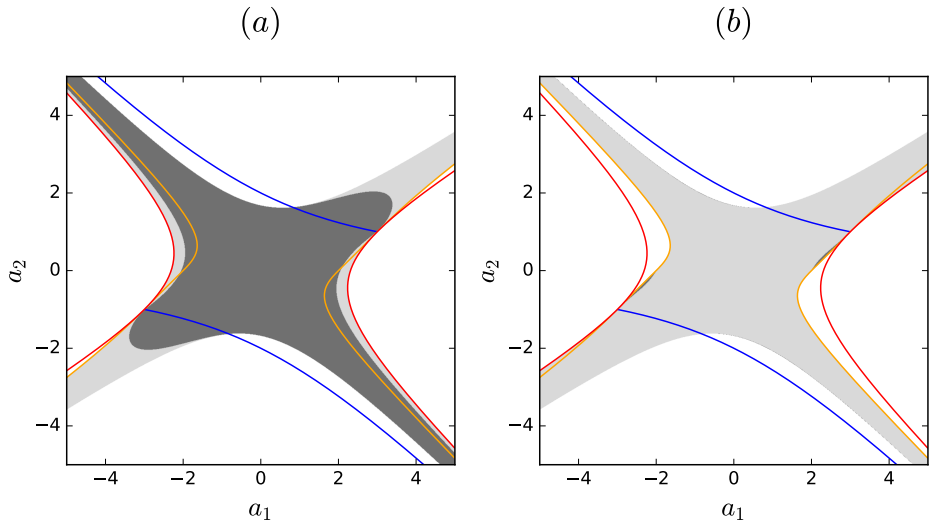

FIG. 6. Stability of the rotating wave selected in the wake of an a_{N+} front (a) and an a_{N-} front (b) in the (a_1, a_2) plane at $\mu = -0.1$. Stable regimes are indicated in dark grey, unstable regimes in light grey, and regions with no front solutions in white. The lines $\Gamma = 0$ (red) and the lines $\Lambda = 6$ (blue) and $\Delta = 0$ (orange) in the region $\Gamma \geq 0$ are also shown.

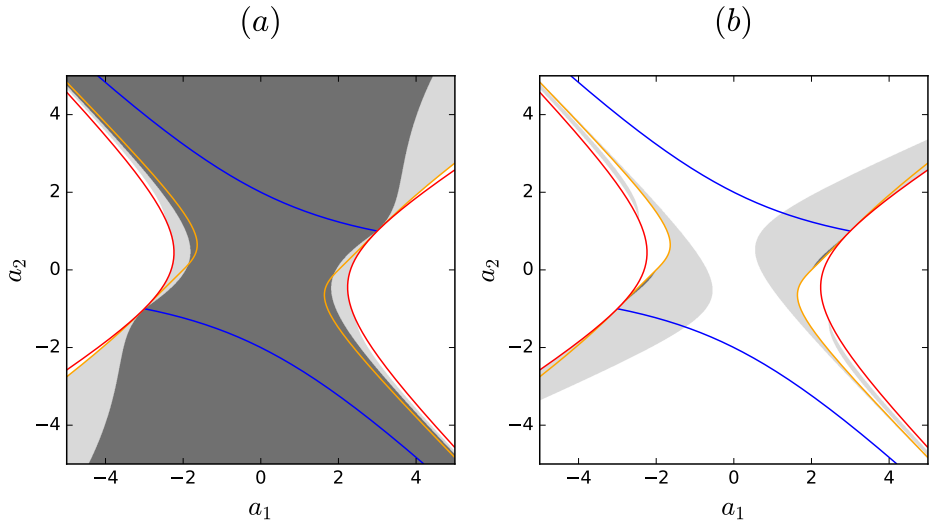

FIG. 7. Stability of the rotating wave selected in the wake of an a_{N+} front (a) and an a_{N-} front (b) in the (a_1, a_2) plane at $\mu = 0.1$. Stable regimes are indicated in dark grey, unstable regimes in light grey, and regions with no front solutions in white. The lines $\Gamma = 0$ (red), $\Lambda = 6$ (blue) and $\Delta = 0$ (orange) in the region $\Gamma \geq 0$ are also shown.

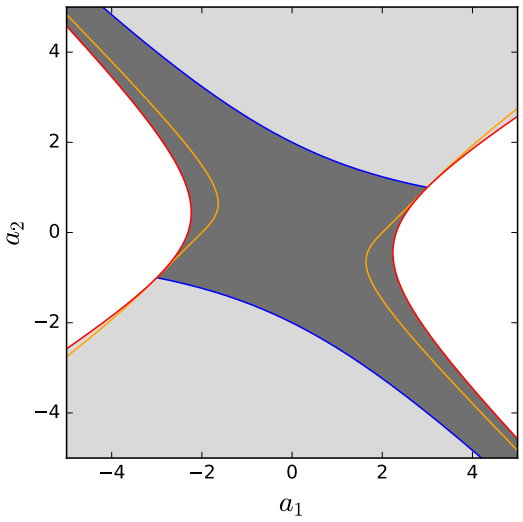

FIG. 8. Stability of the rotating wave selected in the wake of the stationary front at the Maxwell point $\mu = -\frac{3}{\Gamma}$ in the (a_1, a_2) plane. The relevant solution branch is determined by the sign of the quantity $\Lambda - 6$. Stable regimes are indicated in dark grey, unstable regimes in light grey, and regions with no front solutions in white. The lines $\Gamma = 0$ (red), $\Lambda = 6$ (blue) and $\Delta = 0$ (orange) in the region $\Gamma \geq 0$ are also shown.

that characterize the leading edge of the front [19]. The reader is referred to [4] for a comprehensive review of the derivation of this criterion and its applications. Although this criterion relies on linearity it provides accurate predictions for many nonlinear front propagation problems when the front propagates into an unstable state. The criterion is also known to apply to systems that do not admit uniformly traveling profiles, such as the supercritical Swift-Hohenberg equation [21]. These ideas have been employed extensively in the context of fluids [31–33], plasmas [30, 34] and biological systems [35]. In contrast the speed of propagation into a stable state is determined by a nonlinear mechanism and bears no relation to the stability of the state ahead of the front.

In the next two sections we apply these ideas to front propagation in Eq. (1). To validate theoretical predictions we study the evolution of either a localized pulse in the stationary frame or a half-pulse in the moving frame. Specifically, we take two types of initial half-pulses (reflecting in x to get a localized pulse): $A(\xi) = \Theta(-\xi - \ell)$ (Heaviside), where $\Theta(\xi)$ is the Heaviside function and ℓ is a constant, and $A(\xi) = \gamma_1(\xi)e^{i\gamma_2(\xi)}\Theta(-\xi-\ell)$ (random-Heaviside), where γ_1, γ_2 are chosen randomly from uniform distributions on $(0.7, 2)$ and $(0, 2\pi)$, respectively. The latter initial condition is constructed so that it does not select any wave number or amplitude preferentially but still has sufficient amplitude not to decay. Details about the numerical schemes that are used can be found in Appendix C.

IV. FRONT PROPAGATION INTO A STABLE STATE

We turn first to the regime in which the asymptotic state $A = 0$ ahead of the front is stable ($\mu < 0$). We are concerned with the time evolution of localized initial conditions. Since the state $A = 0$ is stable in this regime, the initial condition must be of sufficient amplitude so as to avoid immediate decay back to $A = 0$. When the pitchfork bifurcation to the branch of front states is subcritical and $\mu < \mu_F$ all initial conditions collapse towards $A = 0$. When $\mu_F < \mu < 0$, initial conditions of sufficiently large amplitude typically evolve in their bulk towards one of the stable rotating wave states of Eq. (1) generating a pair of fronts connecting the interior rotating wave at either end to $A = 0$. After an initial transient the fronts travel at a constant speed and in opposite directions. When the pitchfork bifurcation is supercritical the fold always occurs at $\mu > 0$ and the dynamical picture depends more strongly on the parameters. We address specific cases capturing the distinct behaviors that result next.

We find empirically that the selected speed from Heaviside but not random Heaviside initial conditions is correctly predicted by Eq. (13) in many cases, provided that the corresponding solution is stable and the system is known to be well-posed. In Fig. 9 we plot the speed of the two possible fronts, $v_{N\pm}$, as a function of the parameter μ in the subcritical regime for a series of values of the coefficients (a_1, a_2). Figure 9(a) shows the classical case $a_1 = a_2 = 0$ and similar behavior is obtained when one of a_1 or a_2 is increased to 1. For these parameters Heaviside initial conditions evolve on a fast time scale towards the rotating wave corresponding to the stable branch indicated in a continuous blue line and then a pair of fronts propagate outwards at speed $v_{N+} > 0$ expanding the structure, or inwards if $v_{N+} < 0$ contracting the structure. Random Heaviside initial conditions in contrast typically do not approach a fully developed front and instead decay. The red (dashed) part of the velocity curves below the fold corresponds to v_{N-} and these fronts are unstable since they connect to an unstable rotating wave. These findings extend previous results for $(a_1, a_2) = (0, 0)$.

In panel (b) of Fig. 9 we show that the rotating wave selected by Eq. (13) need not be stable. For $\mu < 0$ the curve with parameter values $(a_1, a_2) = (\frac{9}{2}, 4)$ is always unstable while the $(a_1, a_2) = (0, 4)$ solution restabilizes at a finite negative value of μ. In the former case the initial value problem is well-posed and initial conditions appear to decay to $A = 0$. For the $(0, 4)$ solution it is not known whether the initial value problem is well-posed, but when the wave selected by Eq. (13) is stable we observe that Heaviside initial conditions converge to a steady front solution with velocity v_{N+} and random Heaviside initial conditions do not. Also shown in this plot is the case $(a_1, a_2) = (0, 2)$ in which the Maxwell point is located at the fold on the branch of Eq. (13).

Time stepping simulations suggest that solutions initiated at the Maxwell point on this branch are not stable and decay to $A = 0$. Moreover, since the Maxwell point coincides with the fold there is no parameter region in which fronts can contract; amplitude decay occurs when $\mu < \mu_F$ and expansion when $\mu > \mu_F$.

We next turn to some of the cases in which $\Delta < 0$ and only one branch of the front solution exists, persisting for all $\mu < 0$. This branch may be either stable or unstable. In panel (c) of Fig. 9 this is the + branch of the Ansatz and it is stable below some finite $\mu < 0$. For $(a_1, a_2) = (-2, 1)$ and when the predicted velocity $v_{N+} > 0$, we find convergence to the Ansatz solution from both Heaviside and random Heaviside initial conditions. For $(a_1, a_2) = (2.1, 0)$, when the predicted velocity $v_{N+} > 0$ and the solution is unstable, both types of initial conditions converged to a solution with wave number and speed near but not equal to the Ansatz prediction. When $(a_1, a_2) = (2.1, 0)$ the front is predicted to be stable and $v_{N+} > 0$, but we do not observe convergence to this solution unless initial conditions of the form $A(\xi) = e^{iq_N\xi}\Theta(-\xi - \ell)$ are adopted. In both cases when $v_{N+} < 0$ neither Heaviside nor random Heaviside initial conditions evolve towards a steady front. We are able to realize a front moving at speed v_{N+} only with the initial condition $A(\xi) = e^{iq_N\xi}\Theta(-\xi - \ell)$. In panel (d) of the figure a similar bifurcation structure is present but all initial conditions adopted immediately collapsed to $A = 0$. This behavior supports the conjecture of [21] that whenever $v_N < 0$, the selection process is more complex and depends strongly on initial conditions. Furthermore the behavior in the $(a_1, a_2) = (2.1, 0)$ case for which a stable front with a positive velocity is predicted suggests that the system may select a different front solution even when the predicted front is stable. Moreover, the fronts in Figs. 9(c,d) persist as $\mu \to -\infty$, in contrast to previous work. For example, the fronts computed in [12] do not reveal this property because each is computed for a fixed wave number whereas the exact front computed here has a wave number that is μ-dependent. In this case all sufficiently large amplitude initial data with wave number near q_N result in dynamics associated with the + branch of the exact front solution.

V. FRONT PROPAGATION INTO AN UNSTABLE STATE: SPREADING AND MARGINAL STABILITY

When $\mu > 0$ the state $A = 0$ ahead of the front is unstable. In the case of Eq. (1) the spreading speed is easy to calculate but its interpretation is complicated by the nonlinear terms. An application of Eq. (25) to Eq. (1) linearized about the state $A = 0$ leads to the prediction

$$v^* = 2\sqrt{\mu}, \quad q^* = i\sqrt{\mu}, \quad \sigma^* = 2\mu. \tag{26}$$

This result implies that the leading edge of a pulled front takes the form $e^{2\mu t - \sqrt{\mu}x}$ but does not predict the nonlinear state that is left in its wake. The simplest possibility is that front moves at a constant speed in which case $A \equiv A(x - v^*t)$. A necessary condition for this to be the case is that the traveling wave $A = R\, e^{iq(x-v^*t)+i\Im(\sigma^*)t}$ solves the full nonlinear problem for some amplitude R but trails the leading edge of the front [21]. This is distinct from the "node-counting" argument of [18], which is automatically satisfied for fronts that are uniformly propagating. In the present case $q = 0$ and $R^2 = \frac{1}{2}\left(1 + \sqrt{4\mu + 1}\right)$, so this front moving with speed v^* would deposit a zero wave number. This front is excluded, however, whenever $a_1, a_2 \neq 0$: at the location of the front interface $ia_1|A|^2A_x, ia_2A^2\bar{A}_x \neq 0$ and Eq. (1) cannot have a purely real solution. In the following we show that dynamics at the leading edge of the front nonetheless result in the deposition of a state with zero wave number in the wake of a pulled front.

A. Pulled versus pushed: nonlinear selection

In certain cases the selected asymptotic velocity for fronts propagating into unstable states cannot be predicted by the marginal stability criterion and a nonlinear mechanism produces velocities that differ from the linear prediction. This phenomenon, known as "nonlinear selection," was first pointed out in the work of [36]. Nonlinear selection is extensively reviewed in [16] where Eq. (1) is proposed as the most general model for the dynamics near a subcritical steady-state bifurcation. In [16] nonlinear selection is defined as follows: if there exists a front solution with velocity $v^\dagger$ and spatial decay rate $\kappa^\dagger$ that satisfy

$$v^\dagger > v^*, \quad \kappa^\dagger > \kappa^* \tag{27}$$

then this front is established as $t \to \infty$ from localized initial conditions. That is, only under these conditions is a "pulled front" moving at speed v^* not selected and a "pushed front" moving at speed $v^\dagger$ is selected instead. In [21] van Saarloos and Hohenberg conjecture that for a specific class of Ginzburg-Landau equations including (1) the pushed front is precisely that corresponding to Eq. (10) such that $v^\dagger = v_N$ and $\kappa^\dagger = \kappa_N$. This conjecture also requires that the initial conditions have a spatial decay rate not less than $\max\left(\kappa^\dagger, \kappa^*\right)$. These criteria for nonlinear selection are lent mathematical credence by the work of [37]. Specific cases of nonlinear selection are studied rigorously in [29] and lowerbounds on front speeds quantifying violations of linear speed selection are derived in [38, 39] among others. Although a general result characterizing the speed $v^\dagger$ is not known, the wide applicability of the linear criterion determining v^* makes it relatively easy to test the hypothesis in (27) numerically. Here v_N and κ_N have been computed exactly and we analyze all possible selection regimes analytically in

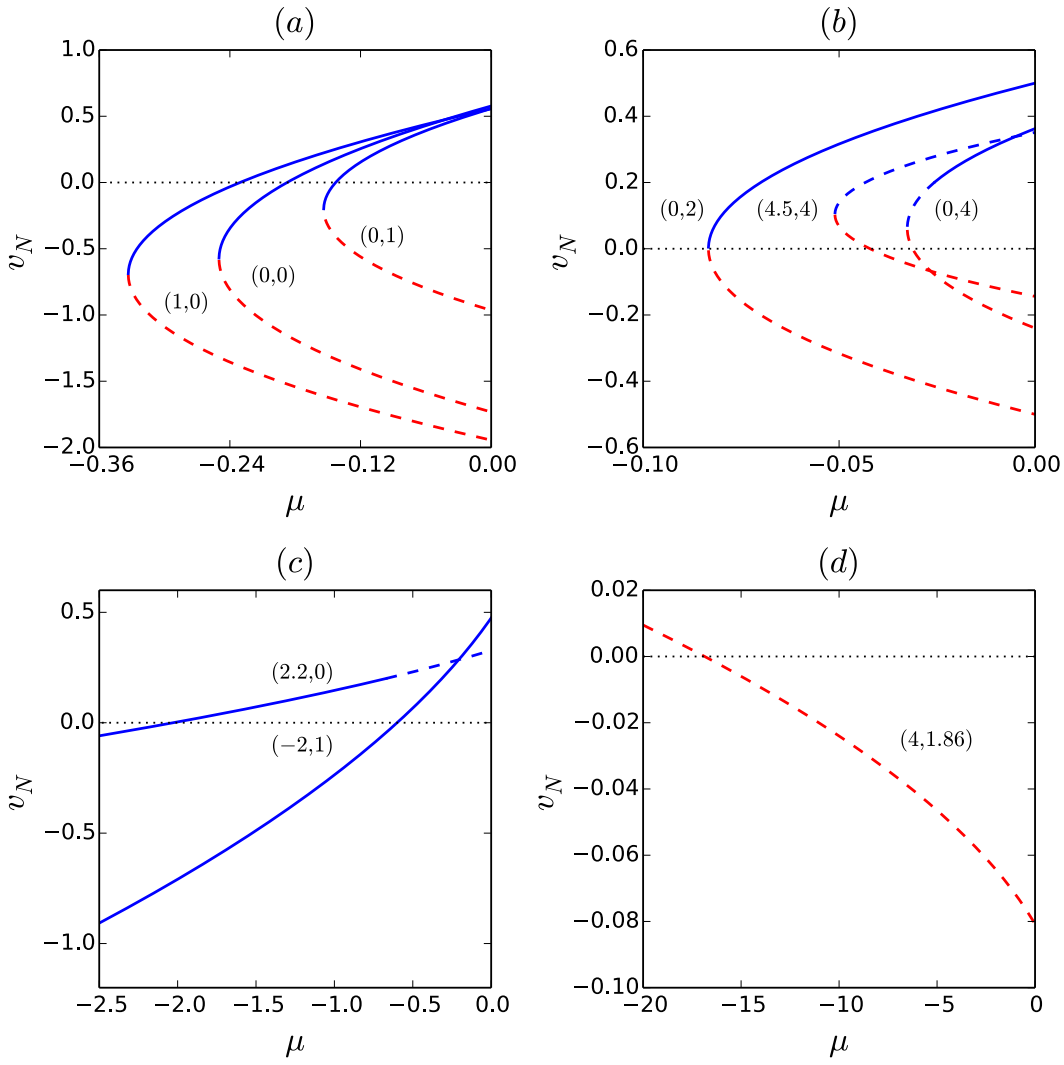

FIG. 9. The velocity $v_{N\pm}$ of the exact front solution is shown in blue and red, respectively. The parameters (a_1, a_2) are indicated next to each curve and dashed lines represent instability of the essential spectrum. The line $v = 0$, shown as a black dashed line, is included for reference.

Appendix B.

Figure 10 shows standard behavior of the front speeds predicted from Eq. (27). The case $(a_1, a_2) = (0, 0)$ is well-studied [19, 23] and is shown in Fig. 10(a). Here the transition from pushed to pulled as determined by (27) occurs at $\mu = \frac{3}{4}$. Although $v_N \geq v^*$ for all $\mu > 0$, the linear decay rate surpasses κ_N at $\mu = \frac{3}{4}$ and remains above it as $\mu \to \infty$. This behavior is typical and validates the intuitive prediction that at high enough forcing all fronts will be pulled. The data points shown in the figure are computed with a finite difference (FD) code and are plotted with an error bar indicating an associated deterministic correction to the speed. Details of this correction and its interpretation can be found in Appendix C. As shown in Fig. 10(b) and (c), v_N and κ_N depend strongly on a_1, a_2 and v_N need not supersede v^* at large μ. We mention that despite the continuity in the speed at the pushed-pulled transition the selected wave number of the deposited state in the wake of the front is generally discontinuous. This "structural instability" has been observed previously in the cubic-quintic complex Ginzburg-Landau equation [21] and appears here generically with the inclusion of either a_1 or a_2.

Fig. 11 shows some nonstandard predictions of Eq. (27) when $a_2 \neq 0$. In Fig. 11(a) the nonlinear front possesses a speed and decay rate that always exceed the linear one. This serves as a counter-example to the suggestion [21] that the linear front will always be selected at sufficiently large μ. In this particular case the decay rate of the selected front is quite small when $\mu \approx 0$. Consequently a very large domain is needed to measure the front speed accurately, significantly larger than our standard domain length $L = 300$. The best results were obtained for Gaussian initial conditions and a spectral method with a domain size $L(\mu)$ determined by the decay rate $\lambda(\mu)$, here $L = 400\lambda(\mu)$ so that $L(0) \approx 1100$. In Fig. 11(b) the nonlinear front has a negative velocity for all $\mu > 0$ where it exists. In this case Eq. (27) does not apply and the asymptotically selected front depends more strongly on initial conditions. We have found that initial conditions in the form of a sharply peaked Gaussian pulse undergo blow-up in finite time, while Heaviside initial conditions decay immediately to $A = 0$. We conjecture that in this parameter regime the Cauchy problem is not well posed. In Fig. 11(c) the nonlinear front Ansatz fails at some finite $\mu > 0$. When μ is larger than this value it is not clear whether the nonlinear terms in the equation saturate for all initial conditions or not. Whereas the case in (b) suffers from blowup we have found that fronts initiated beyond the μ value where the Ansatz fails are well behaved. After an initial transient, Heaviside initial conditions evolve with a leading edge moving at the pulled front speed and deposit a rotating wave with a finite wave number in their wake.

B. The Benjamin-Feir instability and secondary fronts

Further complicating the selection problem is the fact that the dynamically realized front may suffer from secondary instabilities. The deposited rotating wave in the wake of the front can undergo two types of instabilities [13] that may interfere with the propagation of the front. One such possibility is a Benjamin-Feir (BF) instability that generates a state of nonzero wave number. If this instability propagates with a large enough velocity that it overtakes the leading edge of the front, phase slips and spatio-temporal chaos can occur [2, 18, 21, 40].

If the deposited state is unstable to the BF instability then a secondary front inside the deposited state can result. This front is a pulled Kuramoto-Shivashinsky front [4]. In this case there are two regimes corresponding to whether or not the secondary front speed, v_{BF}, is less or greater than the primary one, v. If $v_{BF} < v$ then the deposited pattern behind the primary front grows in size at a rate $v - v_{BF}$ and the instability is advected away from the leading edge. This leads to a double-front structure in the profile of the solution in which the distance between the primary and secondary fronts grows with time [3]. In the second case, $v_{BF} > v$, the instability catches up with the leading edge producing a front whose asymptotic character depends on the existence of stable rotating waves. If the primary front is pushed and the secondary instability deposits a stable rotating wave then a different pushed front results. If the primary front is pulled and the secondary instability deposits a stable rotating wave then phase slips at the leading edge must take place in order that the rotating wave be deposited in the wake of the front. If no stable rotating waves exist then the pulled front may become incoherent [21]. We have searched a variety of regimes in which all rotating waves are unstable but have not observed incoherent pulled fronts. On the other hand incoherent front dynamics can occur for pushed fronts provided the deposited state with wave number q_N is unstable. In the following we elaborate on these notions for both pulled and pushed fronts.

Pulled fronts suffer from secondary instability to phase-winding states with nonzero wave number. The dispersion relation for disturbances to a generic rotating wave state in the stationary frame is provided by Eq. (22) with $v = 0$ and the instabilities only occur when one or both of f, g is non-positive [12, 13]. As shown at the beginning of Sec. V the leading edge of pulled fronts coincides with that of the front that deposits a state of constant amplitude R and zero wave number. Although these fronts cannot be the true pulled fronts for generic values of a_1 and a_2, our observation is that pulled fronts nonetheless deposit a rotating wave with approximately zero wave number in their wake and the necessary phase gradient θ_x (where $u = Re^{i\theta}$) takes the form of a strongly localized pulse at the leading edge. Consequently the prediction of v_{BF} for the zero wave number rotating wave is

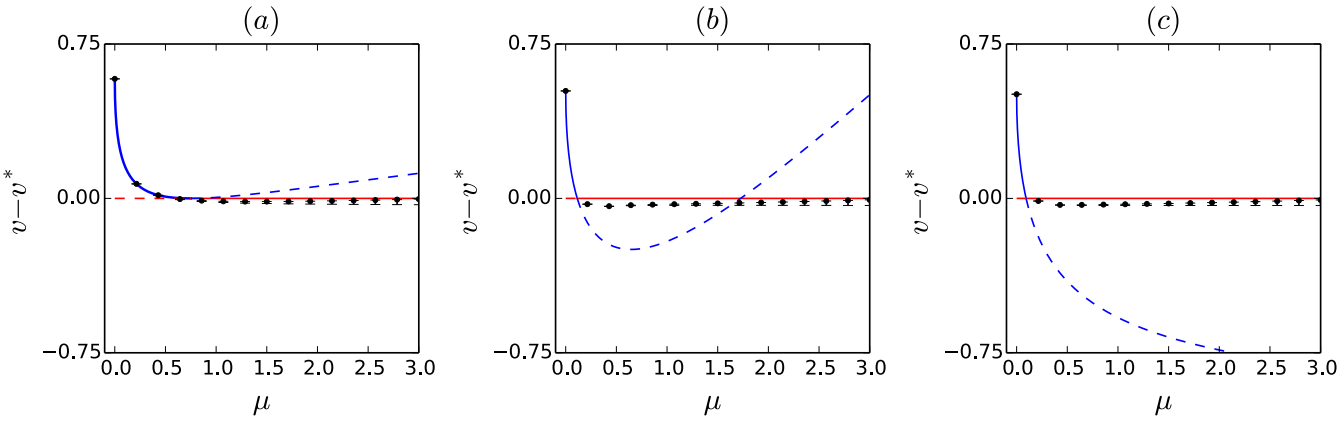

FIG. 10. Front speed v_N (blue) relative to the linear spreading speed v^* (red) for parameters (a_1, a_2): (a) $(0, 0)$, (b) $\left(-\frac{8}{5}, \frac{1}{2}\right)$, (c) $\left(\sqrt{\frac{8}{3}}, 0\right)$. The selected (not selected) speed is indicated by a solid (dashed) line according to Eq. (27). The black dots represent speeds calculated by time-stepping Heaviside initial conditions with FD in the stationary frame and tracking the motion of the front. The space and time discretizations are $\Delta x = 0.05$ and $\Delta t = (\Delta x)^2$, further details are contained in Appendix C. The deterministic corrections as a result of the FD approximation (computed in Appendix C) are shown using error bars on the points.

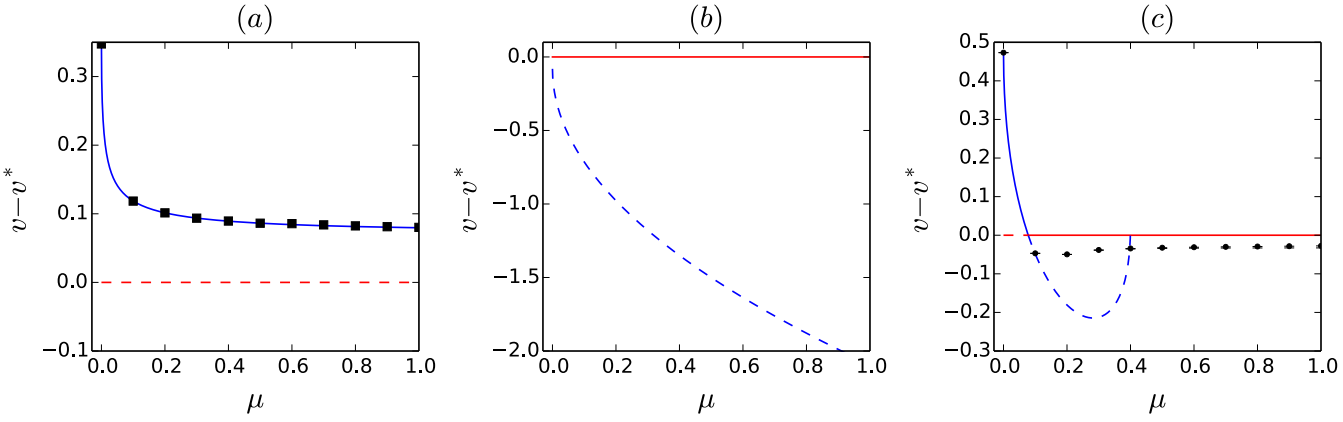

FIG. 11. Front speed v_N (blue) relative to the linear spreading speed v^* (red) for parameters $(a_1, a_2, \pm)$, where the symbol $\pm$ specifies the front: (a) $(-15, 16, +)$, (b) $(4, 1.86, -)$, (c) $(-2, 1, +)$. The selected (not selected) speed is indicated by a solid (dashed) line according to Eq. (27). The black squares represent speeds calculated in a domain of length $L = 400\lambda$ by time-stepping Gaussian initial conditions in the stationary frame using a spectral method with parameters $\Delta t = 0.01$, $N_x = 4096$ and $\epsilon = 8$ (Appendix C). The black dots represent speeds calculated by time-stepping Heaviside initial conditions in the stationary frame using a finite difference (FD) code with space and time discretizations $\Delta x = 0.05$, $\Delta t = (\Delta x)^2$, and tracking the motion of the front (Appendix C). The deterministic corrections as a result of the FD approximation (computed in Appendix C) are shown using error bars on the points.

a good estimate for the speed of pulled fronts undergoing this secondary instability.

The zero wave number rotating wave has $f = \left(4 + a_2^2 - a_1^2\right) R^4 - 2R^2$, $g = 2\mu + R^2$, where $R^2 = \frac{1}{2}\left(1 + \sqrt{4\mu + 1}\right)$. When $\mu > 0$ one can show that $g > 0$ always but $f > 0$ only if $a_1^2 - a_2^2 < 2$. The state suffers from instability when $a_1^2 - a_2^2 \geq 4$ for any positive μ, and when $4 > a_1^2 - a_2^2 > 2$ for $0 \leq \mu < \frac{2(a_1^2 - a_2^2 - 2)}{(4 - a_1^2 + a_2^2)^2}$. Applying the marginal stability criterion to the dispersion relation for the secondary instabilities produces a prediction for the front speed, wave number, and frequency of the secondary front. This calculation is shown explicitly at the end of Appendix A. We discuss an application next.

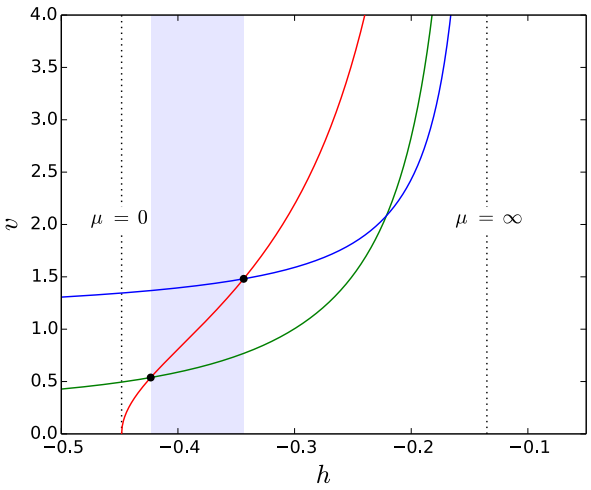

FIG. 12. Speeds v^* (red), v_N (green), and v_{BF} (blue) for pulled fronts as a function of the variable h defined in Appendix A 3 for $(a_1, a_2) = \left(\frac{5}{2}, 1\right)$. Increasing h corresponds to increasing μ. The parameters corresponding to $\mu = 0, \infty$ are indicated with dotted lines and the region in which pulled fronts are selected **and** $v_{BF} > v^*$ is delimited by blue shading. The transition from pushed to BF-unstable pulled fronts, and subsequently from BF-unstable to BF-stable pulled fronts is marked by black dots.

As an example we consider the case $(a_1, a_2) = \left(\frac{5}{2}, 1\right)$ and plot the velocities v^*, v_N, and v_{BF} in Fig. 12. For this figure we plot velocities as a function of a variable h which is an order-preserving one to one reparametrization of μ and depends on a_1 and a_2. The choice of $h(\mu)$ arises naturally in the calculation of v_{BF} and is defined in Appendix A. In this plot the BF velocity corresponds to instabilities of the zero wave number rotating wave and not the rotating wave left in the wake of the nonlinear front. The rotating wave for the nonlinear front Ansatz is stable for $\mu \lesssim 5$, throughout the pulled-pushed crossover. After the transition occurs from pushed to pulled at $\mu \approx 0.072$ (left black dot), $v_{BF} > v^*$ and the pulled front is unstable. This is shown in Fig. 13 with $\mu = 0.4$ (raised above threshold for clarity) and the prediction of the leading edge motion based on the speed v^* is shown in red. After a transient, the front propagates at the linear spreading speed but deposits a nonzero wave number approximately equal to q_N. This is enabled by phase slips at the leading edge. By $\mu \approx 0.55$ (right black dot) the pulled front restabilizes as its speed exceeds that of the BF instability for the zero wave number rotating wave. This phenomenon is pictured in Figs. 15 and 14 ($\mu = 1$) in which the speeds v^* and v_{BF} are shown in red and blue, respectively. The primary front deposits a state with near-zero wave number followed by a secondary front that generates a larger amplitude asymptotic state with a different wave number in its wake, but still close to q_N. The separation of the primary and secondary fronts hearkens to the double front structure observed in [3].

Figures 13 and 14 also reveal two features at the leading edge that we cannot predict theoretically. First is the periodic nucleation of amplitude holes or "grooves" whose profile is shown in Fig. 15. These holes increase and then decrease in depth as time passes eventually merging with the otherwise homogeneous amplitude state left in the wake of the front. In the case of Fig. 13 the time scale on which the holes anneal is much longer than the time scale for the front propagation and the holes therefore grow in number as the front propagates. In the case of 14 the holes vanish on a comparable time scale to the primary front and thus only one is present at any given time. This phenomenon can also be seen in Figs. 16 and 17 at the secondary front interface and has been verified using both FD and Fourier discretizations. This feature has also been observed in [3] in a nonvariational case, although there the holes, once nucleated, do not disappear. The second feature visible in both figures is the presence of phase slips. These occur at the leading edge of the front in Fig. 13 and at the edge of the secondary front (which we suspect is also pulled) in Fig. 14. These phase slips occur at the spatial location of the holes and at the time when the holes reach their greatest depth. These locations correspond to the darkest points along the hole trajectory in a space-time plot of $|A(x,t)|$. The phase slips are not a surprise, since the leading edge dynamics for pulled fronts are set by the linearization about the unstable state and these may not generate in their wake a stable solution to the nonlinear problem. The eventual wave number that is deposited by the passage of the front is near q_N throughout the domain but modulated on a much larger length scale.

Turning now to pushed fronts, we compute the velocity of propagation for the BF instability around an arbitrary phase-winding state deposited in the wake of the front Eq. (10). Although this analysis was carried out in [13], we generalize it and show that there are additional solutions to the marginal stability equations for type I instabilities that have not been previously reported. The details of this calculation are included in Appendix A. There are two broad instability regimes for pushed fronts depending on whether the far-field marginal wave number has a nonzero (type I) or zero (type II) real part.

We first discuss the case of instability to perturbations

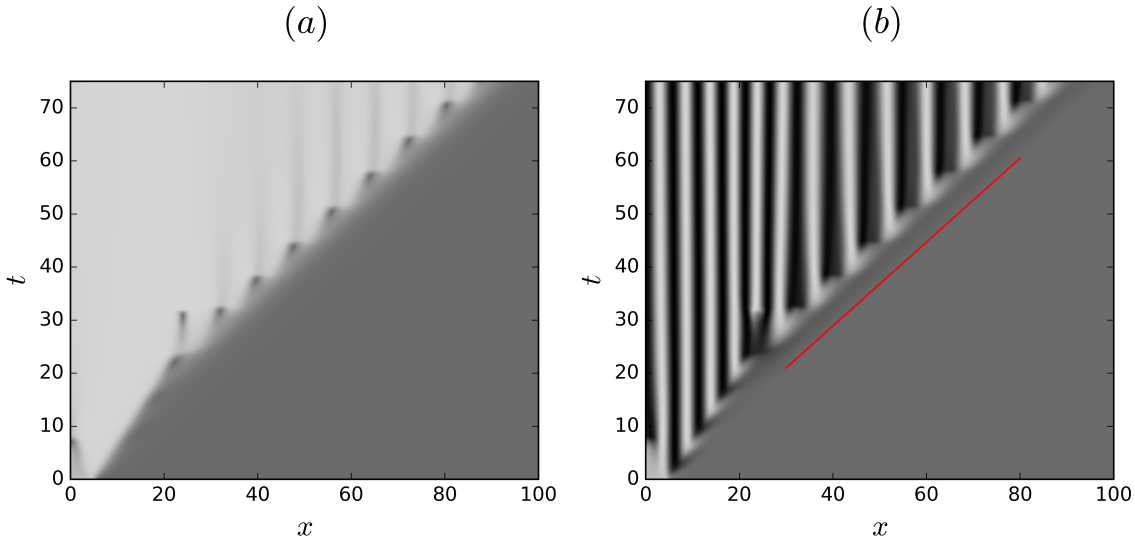

FIG. 13. Space-time plot of the evolution of (a) $|A(x,t)|$ and (b) $\Re[A(x,t)]$ from Heaviside initial conditions in the stationary frame for $(a_1, a_2) = \left(\frac{5}{2}, 1\right)$ and $\mu = 0.4$ computed using FD. The calculation is done on a domain $[-100, 100]$ with Dirichlet boundary conditions on both $\Re(A)$ and $\Im(A)$ and only half of the simulation window is shown. The space and time discretizations are $\Delta x = 0.2$ and $\Delta t = 0.0025$. In this regime after an initial transient the front is pulled, traveling at speed v^* to a good approximation. An offset line representing propagation at speed v^* is shown in red.

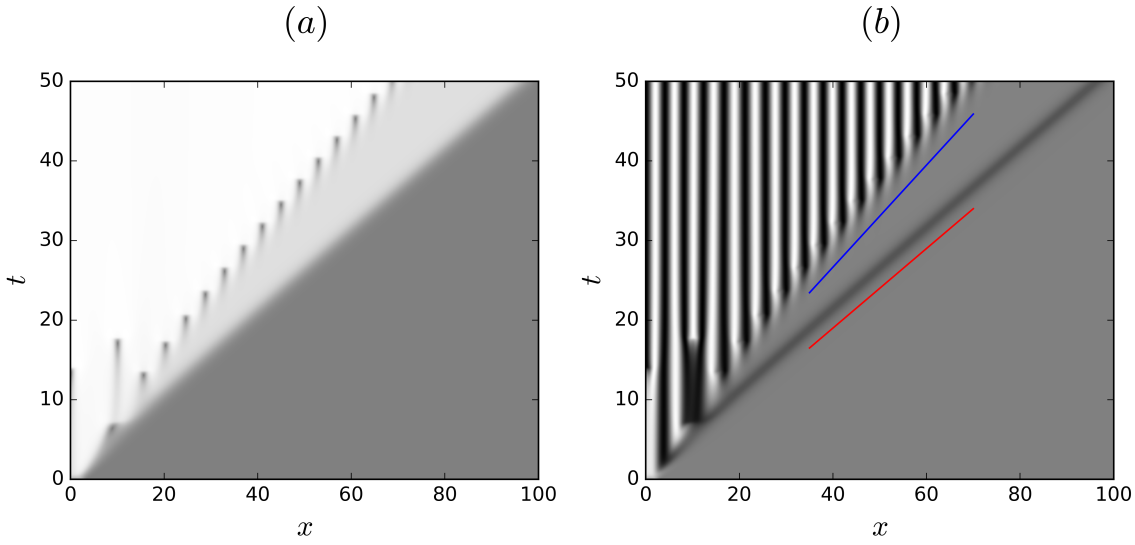

FIG. 14. Space-time plot of the evolution of (a) $|A(x,t)|$ and (b) $\Re[A(x,t)]$ from Heaviside initial conditions in the stationary frame for $(a_1, a_2) = \left(\frac{5}{2}, 1\right)$ and $\mu = 1$ computed using FD. The calculation is done on a domain $[-100, 100]$ with Dirichlet boundary conditions on both $\Re(A)$ and $\Im(A)$ and only half of the simulation window is shown. The space and time discretizations are $\Delta x = 0.1$ and $\Delta t = 0.005$. In this regime after an initial transient the front is pulled, traveling at speed v^* and a secondary front separates from the leading edge traveling at a speed v_{BF}. Offset lines representing propagation at speeds v^* (red) and v_{BF} (blue) are also pictured.

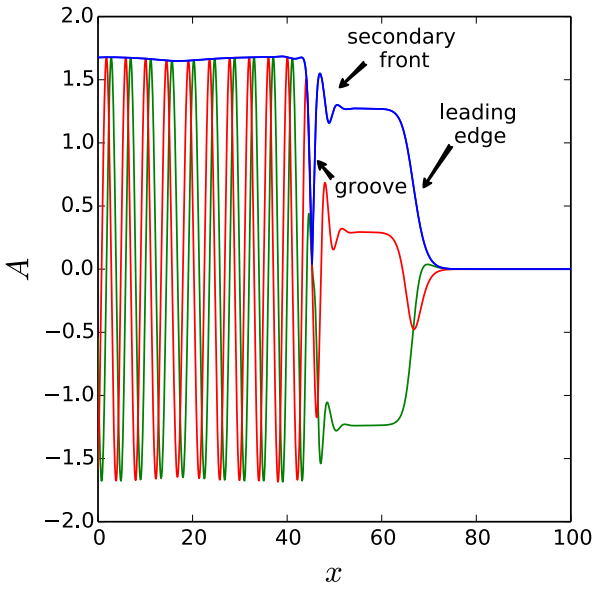

FIG. 15. Solution $A(x, t = 35)$ computed from Heaviside initial conditions in the stationary frame using FD for $(a_1, a_2) = \left(\frac{5}{2}, 1\right)$ and $\mu = 1$, showing $\Re(A)$ (green), $\Im(A)$ (red) and $|A|$ (blue) on half of the computation domain. The discretization parameters are $\Delta x = 0.1$ and $\Delta t = 0.005$.

with a wave number of finite real-part at onset, type I. This case includes the parameter values $(a_1, a_2) = \left(\frac{5}{2}, 1\right)$ of the previous discussion but not near $\mu = 0$ where a pushed front is predicted. In order to find finite wave number instability near $\mu = 0$ we must choose parameters in the region $\Delta < 0$ and so select $(a_1, a_2) = \left(-2, \frac{1}{2}\right)$. The corresponding far-field rotating wave is unstable for $\mu \in (-0.1888, 0.5184]$. An evolution plot for Heaviside initial data at $\mu = 0$ is shown in Fig. 16 in a frame moving at speed v_N. The initial data are immediately unstable to a traveling wave which is advected leftwards relative to the primary front moving at speed v_N to the right. Simultaneously the leading edge of the front generates a distinct rotating wave with a wave number *exactly* equal to q_N as can be seen from Fig. 17 in which we plot the amplitude $\tilde{A}(\xi, t)$ that omits the wave number of the primary rotating wave (Appendix C). The resulting secondary front between these two rotating waves is slower than the primary one indicating that the secondary front instability is convective in the frame moving at speed v_N and so separates from the leading edge. Our prediction for the secondary front speed, v_{BF}, can be checked by transitioning to a frame moving at that speed as shown in Fig. 17. Because the rotating wave in the wake of the primary front has not been restored in this plot the secondary front can be clearly distinguished. After a transient the secondary front is stationary in this frame and generates a rotating wave behind the primary one with a different wave number.

The case of instability with respect to perturbations with asymptotically zero wave number (type II) is realized when $(a_1, a_2) = (\frac{9}{2}, 5)$. This corresponding far-field rotating wave exhibits instability for $\mu \in [-0.0283, 0.1087)$. When $\mu < 0$ Heaviside initial data decay to $A = 0$ but for $\mu > 0$ a front subsists. A space-time plot is shown in Fig. 18. Initially a rotating wave born at the front interface invades the initial condition to the left, leaving an amplitude gradient across the structure. The invasion is largely complete by $t \approx 500$ and the resulting state persists over a long time scale, until $t \approx 1000$. At this point an amplitude perturbation grows to such an extent that it triggers an abrupt collapse of the structure. Since $\mu > 0$ the $A = 0$ solution is unstable, and the remnant of the front near the leading edge generates a sequence of traveling pulses that break-up into an interval of spatio-temporal chaos ($1000 \lesssim t \lesssim 1800$). Near $t \approx 1800$ the chaos abruptly subsides and the most of the original front is restored. This state persists for a few hundred timesteps or so before it collapses again. The longer time series shown in Fig. 19 shows that this is part of a recurrent process with alternating coherent and incoherent episodes. The space-time plots demonstrate that the primary front travels at the predicted speed v_N when the deposited state is coherent but that the front is slightly delayed when the deposited state is incoherent. We cannot predict the front speed in these chaotic intervals. Figure 20 provides another perspective on the chaotic behavior shown in Fig. 19. The figure shows the time series $|A(\xi = 100, t)|$ and highlights the abrupt collapse episodes towards $|A| \approx 0$ that trigger the intervals of spatio-temporal chaos, before the system returns to coherence. It is noteworthy that even in the coherent phase the amplitude $|A|$ always initially overshoots the target amplitude a_N and thereafter decreases, ultimately triggering a collapse episode.

Since the secondary instability is of type II we can easily compute $v_{BF} \approx 1.878$ using the methods in [13]. This speed is much greater than both the frame speed $v_N \approx 0.3623$ and the linear spreading speed $v^* \approx 0.3162$ and so the secondary instability quickly catches up with the front. The speed v_{BF} is indicated in Fig. 19 as an offset blue line and shows good agreement to the observed speed at which large amplitude perturbations impact the front triggering the onset of incoherent front propagation. In contrast, the speed between the $u \approx 0$ amplitude holes behind the leading edge and the spatio-temporally chaotic state is also well defined but cannot be predicted with our methods. It is also worth noting that in the intervals of incoherent motion the leading edge of the front propagates neither at v_N nor v^*. If the episodic breakdown of the front exhibited in Fig. 19 persists for all time it would generate a counterexample to the nonlinear marginal stability conjecture of van Saarloos and Hohenberg that the front must in the long time limit propagate at the predicted speed, v_N [21].

We were unable to find parameter regimes for which $v_{BF} > v_N$ in the pushed front regime and the secondary instability was of type I. This would be an interesting case since it is not clear what would happen to the pri-

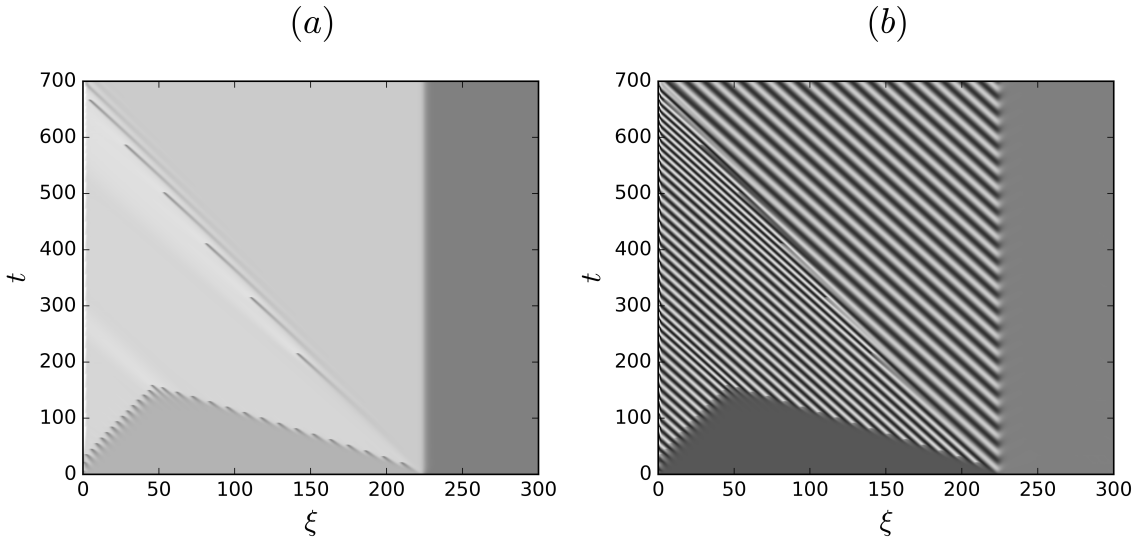

FIG. 16. Space-time plot of the evolution of (a) $|A(\xi,t)|$ and (b) $\Re[A(\xi,t)]$ from Heaviside initial conditions in the moving frame for $(a_1,a_2)=\left(-2,\frac{5}{2}\right)$ and $\mu=0$. The speed of the moving frame is v_N and the front is pushed. In this simulation we use time step $\Delta t=0.01$, number of Fourier modes $N_x=6144$, and cutoff exponent $\epsilon=10$.

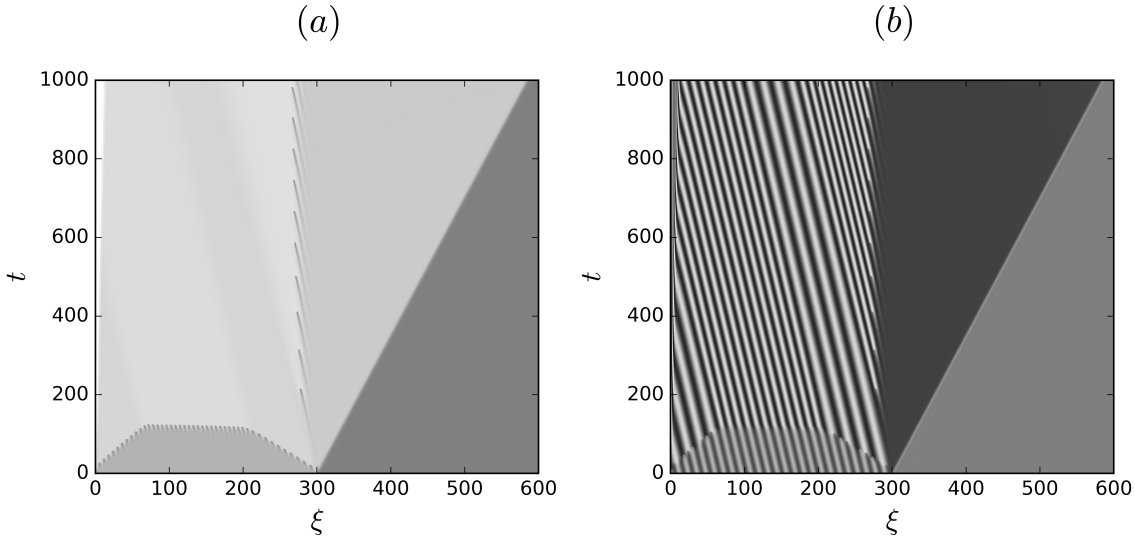

FIG. 17. Space-time plot of the evolution of (a) $|\tilde{A}(\xi,t)|$ and (b) $\Re[\tilde{A}(\xi,t)]$ from Heaviside initial conditions in a frame moving at speed v_{BF} for $(a_1,a_2)=\left(-2,\frac{5}{2}\right)$ and $\mu=0$. In this simulation we use time step $\Delta t=0.005$, number of Fourier modes $N_x=6144$, and cutoff exponent $\epsilon=10$.

mary front velocity. In the pushed case the front velocity depends on a nonlinear mechanism and is affected by the rotating wave in the wake of the front. If an instability overtakes the front thereby changing it to one outside of the family described by the Ansatz would the speed change? The search for this situation is nontrivial because for every different choice of (a_1, a_2) one must recompute and invert the function $h(\mu)$ whose branches must in general be chosen by hand (Appendix A), evaluate v_{BF} on the appropriate elliptic curve and write v_N in terms of h on each branch. As a result it is not straightforward to scan parameter space.

VI. DISCUSSION

In this paper we analyze in some considerable detail the properties of fronts connecting a stripe pattern to a spatially homogeneous state. For this purpose we use the generic amplitude equation describing a weakly subcritical bifurcation to the pattern state. For $\mu < 0$ (the subcritical regime) this equation exhibits bistability between the pattern and the homogeneous state implying that the speed of the front is determined by nonlinear processes. Fronts of this type are called *pushed* fronts. In contrast, in the supercritical regime ($\mu > 0$) the homogeneous state is unstable and the marginal stability criterion of Dee and Langer [18] then suggests that sufficiently localized initial conditions evolve into an invasion front whose speed is selected by linear processes. Such fronts are *pulled*.

To examine these predictions and the transition between them as the bifurcation parameter μ varies we construct a class of exact nonlinear front solutions with an explicit expression for the front speed. In the subcritical regime this speed vanishes at an analogue of a Maxwell point, corresponding to the presence of a heteroclinic connection between the stripe state and the homogeneous state. These exact solutions extend into the supercritical regime and the question arises therefore as to when the marginal stability criterion prevails. This question is addressed already in the work of van Saarloos [16] (see also [23]) but only for the special case when the coefficients (a_1, a_2) both vanish, and the system exhibits gradient dynamics. This early work highlighted the fact that pushed fronts, propagating at v_N, do indeed persist well into the supercritical regime and are dynamically selected by localized initial conditions. Our work extends this result to cases where (a_1, a_2) are nonzero and shows that (i) the linear stability mechanism does indeed prevail for sufficiently large μ and most values of (a_1, a_2), i.e., that for $0 < \mu \leq \mu^{\ddagger}(a_1, a_2)$ nonlinear speed selection does indeed take place while the speed is selected by linear processes only for $\mu > \mu^{\ddagger}(a_1, a_2)$, and that (ii) there exist parameters (a_1, a_2) for which $\mu^{\ddagger}(a_1, a_2) = 0$ and others for which $\mu^{\ddagger}(a_1, a_2) = \infty$. Examples of these degenerate cases are shown in Fig. 11(a),(b). In Appendix B we show that options (i) and (ii) are the only ones that can occur and obtain the conditions on (a_1, a_2) for the presence of degeneracies mentioned above. These conditions are complicated, but can in principle be replotted in the (a_1, a_2) plane. In particular, we show that the speed selection inequalities do not allow the selection of a nonlinear front after the first transition from pushed to pulled ($\mu > \mu^{\ddagger}(a_1, a_2)$).

In fact, the details of the transition from pushed to pulled fronts are complex since the selection process depends on the steepness of the initial solution profile, and the stripe state deposited in the wake of the moving front may or may not be stable. We emphasize that the wave number of this state is selected dynamically and is not in general the equilibrium wave number k_c of the underlying pattern. As a result the deposited state is susceptible to secondary instabilities. These are of Benjamin-Feir type and may be convective or absolute in the frame of the front [2]. The former do not disrupt the stripe state since the growing perturbations are advected away from the front, but in the latter case the instability manifests itself in the vicinity of the front and may lead to its disruption. We have exhibited several examples where the front undergoes episodic complex time-dependence that we attribute to this process. Specifically, we have identified four distinct processes that bear on the wave number of the invading stripe state:

- The wave number becomes $k_c + \epsilon q_N$ if the front is pushed and the rotating wave with this wave number is stable,
- The wave number remains k_c when the front is pulled and $v_{BF} < v^*$, where v_{BF} corresponds to the secondary instability of the invading k_c state,
- We do not have an analytical prediction of the wave number if the front is pulled and $v_{BF} > v^*$ and the secondary instability interacts with the original k_c front, although it appears to remain near $k_c + \epsilon q_N$ despite the presence of phase slips,
- We do not have an analytical prediction of the wave number if the front is pushed and $v_{BF} > v_N$, where v_{BF} is now the speed of the secondary front generated by instability of the $k_c + \epsilon q_N$ front; in the example shown in Fig. 11(a) the intermittent dynamics of the front preclude the selection of an asymptotic wave number.

Our work provides a detailed discussion of the different regimes that may be encountered as one traverses the (a_1, a_2) parameter space. We believe that some of the conditions required for the applicability of the Ansatz are likely related to the conditions for well-posedness of the non-gradient system $a_2 \neq 0$. We have not, however, studied instabilities associated with unstable point eigenvalues in the spectrum of the front but note that these, if present, may lead to rich dynamics localized at the front. Evidently much remains to be learned about problems involving the invasion of one state by another, even in situations as simple as that studied here.

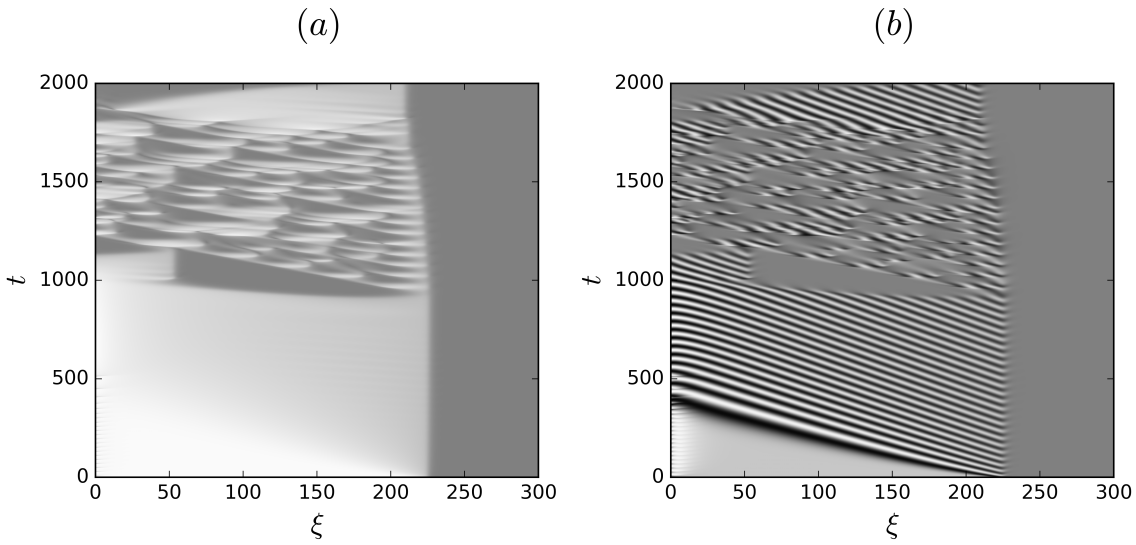

FIG. 18. Space-time plot of the evolution of $A(\xi, t)$ from Heaviside initial conditions in the moving frame for $(a_1, a_2) = (\frac{9}{2}, 5)$ and $\mu = 0.025$. The speed of the moving frame is v_N and the front is pushed. In this simulation we use time step $\Delta t = 0.01$, number of Fourier modes $N_x = 3072$, and cutoff exponent $\epsilon = 5$.

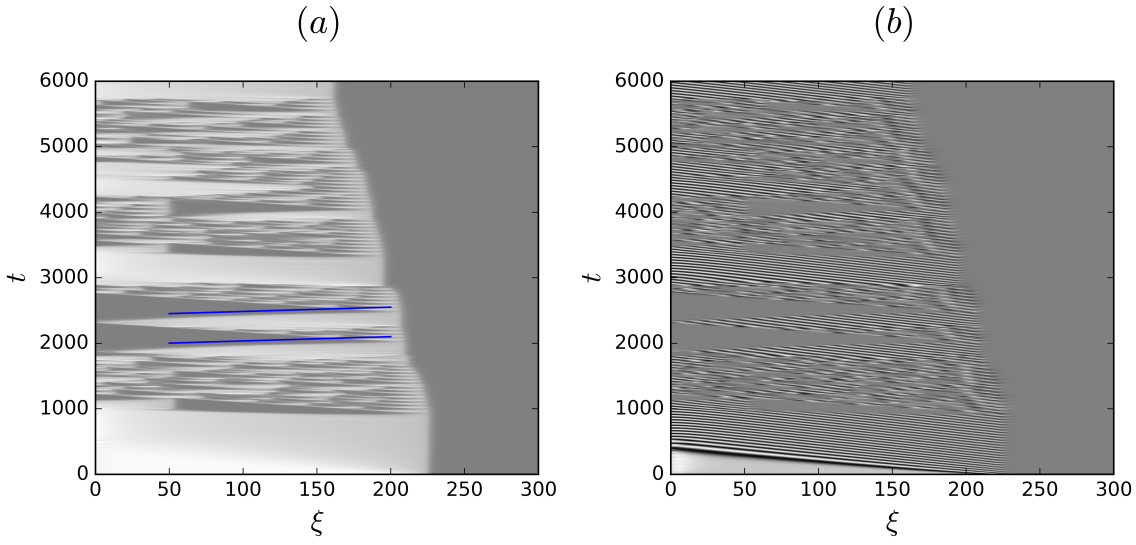

FIG. 19. Continuation of the space-time plot in Fig. 18 over a longer time interval with an initial condition of different amplitude. Offset lines representing propagation at speed v_{BF} (blue) are also pictured.

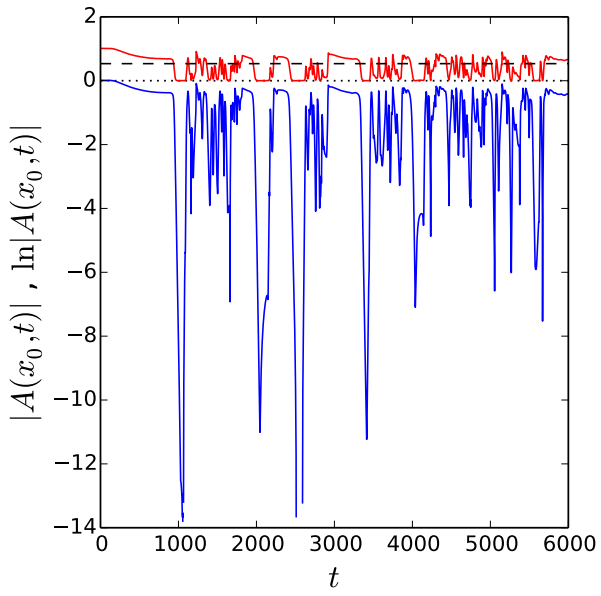

FIG. 20. Time-series of $|A(\xi_0,t)|$ (red) and $\ln|A(\xi_0,t)|$ (blue) representing a vertical slice of the evolution shown in Fig. 19 at $\xi_0 = 100$. The amplitude $A = a_N$ is plotted with a thick dashed line (black) and $A = 0$ is also shown for reference.

ACKNOWLEDGEMENTS

The authors would like to thank Eric Larson for insightful discussions about polynomial equations and Ryan Goh for helpful discussions on the computation of eigenvalue spectra. This work was supported by the National Science Foundation under grant DMS-1613132.

Appendix A: Benjamin-Feir instability

This appendix is devoted to finding *all* solutions of Eq. (25) obtained from the dispersion relation for perturbations of nonlinear rotating wave solutions of Eq. (1). Because the marginally unstable wave number, q^*, is generically complex the dispersion relation can exhibit branch cuts and complicated dependance on the phase of the radicand. These properties render the task of solving the marginal stability equations analytically in their standard form intractable and their numerical solution unstable. In this section we instead transform these equations into polynomial equations and show that after appropriate transformations *all* the solutions lie along a unique elliptic curve. We thus provide an explicit parametrization of the solution curves and provide a numerically tractable route to computing the desired front velocity. The entirety of the calculation is done in the stationary frame and we are particularly interested in the velocity v_{BF} selected by secondary (Benjamin-Feir) instabilities.

Before analyzing the generic case, we note that there are two nongeneric situations that can occur, corresponding to $2g - f = 0$ and $g = 0$, respectively. When $g = 0$ the dispersion relation reads $\sigma = \pm\sqrt{-fq^2} - q^2$ and for each sign of the root there are four cases to consider depending on the sign of f and the quadrant of q. In each case we solve the marginal stability equations in the original variables to verify that q lies in a consistent quadrant. In the table below we take the positive root.

sgn(f)	quadrant of q	σ	solution of Eq. (25)
-1	1 , 4	$\sqrt{\|f\|}q - q^2$	$q^* = \frac{\sqrt{\|f\|}}{2}(1 \pm i)$
-1	2 , 3	$-\sqrt{\|f\|}q - q^2$	$q^* = \frac{\sqrt{\|f\|}}{2}(-1 \pm i)$
1	1 , 2	$-i\sqrt{\|f\|}q - q^2$	$q^* = 0$
1	3 , 4	$i\sqrt{\|f\|}q - q^2$	$q^* = 0$

As shown in the table, the first two cases are consistent while the second two are not. Since the case of the negative root is obtained by switching the dispersion relations and q values of rows $1 \leftrightarrow 2$ and $3 \leftrightarrow 4$, there is no consistent case and hence no solution for the branch with negative root. In the case $2g = f$ the dispersion relation is $\sigma = \pm|g| - g - q^2$ and the condition $\Re[\sigma'(q)] = 0$ implies $q_r = 0$ so that $q^* = i\sqrt{|g| - g}$.

In the general case ($f \neq 2g$, $g \neq 0$) we work in terms of the parameters $c = \frac{g}{2g-f}$, $d = \frac{1}{cg}$ and we define $\theta(q)$ via

the relation $\sigma(q) = \frac{\theta(q)+c-1}{cd}$. We also introduce the shorthand notation $s_z \equiv \mathrm{sgn}(z)$. The condition (25) becomes

$$\Re\left[\theta'\right] = 0, \qquad -\Im\left[\theta'\right]\Im[q] = \Re\left[\theta\right] + c - 1, \qquad \Im[q] > 0, \tag{A1}$$

along with the obvious requirement $\Re[\sigma] > 0$. With the introduced parameters and relation (22) we have

$$\theta = \pm s_g\sqrt{dq^2+1} - c\left(dq^2+1\right), \quad \theta' = \pm s_g\frac{dq}{\sqrt{dq^2+1}} - 2cdq. \tag{A2}$$

To resolve the branches in $\sqrt{dq^2+1}$, consider the holomorphic substitution $q = \frac{2t}{\sqrt{|d|}(s_d - t^2)}$ which parametrizes both branches in t but double-counts the physically irrelevant point $q = 0$ at $t = 0$ and ∞. With this substitution the argument of square roots becomes the square of $\frac{s_d+t^2}{s_d-t^2}$. Letting $t = x + iy$, where $x, y \in \mathbb{R}$, it becomes clear that x and y always appear squared in the relevant parts of Eq. (A1). Thus we are free to choose their sign such that $\Im\left[\frac{s_d+t^2}{s_d-t^2}\right] > 0$. Eliminating the square roots produces

$$s_g\theta = \frac{\frac{1}{2}\frac{h+s_d}{h-s_d}\left(t^2+s_d\right)^2 \pm \left(1-t^4\right)}{\left(t^2-s_d\right)^2}, \qquad \frac{s_g\theta'}{\sqrt{|d|}} = \begin{cases} \frac{4t}{h-s_d}\frac{h+t^2}{1-t^4} & (+) \\ \frac{4s_dt}{h-s_d}\frac{1+ht^2}{1-t^4} & (-) \end{cases}, \tag{A3}$$

where h is a real variable defined by

$$h \equiv \frac{2\left|c\right| - s_d}{2\left|c\right| s_d + 1}.$$

Since the factor $\sqrt{|d|}$ cancels out in the equation for $\Im[\theta']$, the change of variables reduces a 4-parameter problem (q, f, g) into a 3-parameter problem (t, h) with eight cases depending on s_d and s_g and the sign of the root.

1. First condition

We are now prepared to begin resolving the condition $\Re\left[\theta'\right] = 0$ and focus first on the positive root. In the (t, h) variables this reduces to

$$\Re\left[\frac{t\left(h+t^2\right)}{1-t^4}\right] = 0. \tag{A4}$$

We now proceed by clearing all denominators under the assumption that they do not vanish and return to nongeneric points like $t = \sqrt{i}$ later. Setting $t = x + iy$, relation (A4) expands to

$$x\left\{h\left(x^4 - 2x^2y^2 - 3y^4 - 1\right) + \left(x^2+y^2\right)^3 - x^2 + 3y^2\right\} = 0. \tag{A5}$$

Note that the trivial condition $x = 0$ results in a purely imaginary t and this is the well-known solution with purely imaginary q [13]. In addition to this solution there is a set of solutions with nontrivial x and it is those solutions that we consider in what follows.

When $x \neq 0$ Eq. (A5) is a polynomial in even powers of x and y. Introducing $u = x^2$ and $v = y^2$ we obtain

$$u = \frac{1}{4}\left(\frac{h-k^3}{hk-1} + 3k\right) \tag{A6}$$

with $k = u + v$. The case of $h = \pm 1$ in which there are extra solutions $k = \pm 1$ is included in the set of nongeneric cases that are discussed above at the beginning of the section.

As for the negative root, the relation $\Re\left[\frac{t\left(1+ht^2\right)}{1-t^4}\right] = 0$ gives

$$x\left\{3y^4\left(hx^2-1\right) + y^2\left(3h\left(x^4+1\right) - 2x^2\right) + \left(x^4-1\right)\left(hx^2+1\right) + hy^6\right\} = 0. \tag{A7}$$

Ignoring the case $x = 0$, the other factor may be written in terms of (u, k) as

$$u = \frac{1}{4}\left(\frac{hk^3 - 1}{h - k} + 3k\right). \tag{A8}$$

From here we work in the (h, k) variables where k remains to be set by the second condition in Eq. (A1).

2. Second condition

The second condition in Eq. (A1) for the positive root can be written as

$$-\frac{8s_g}{h - s_d}\Im\left[\frac{t\left(h + t^2\right)}{1 - t^4}\right]\Im\left[\frac{t}{s_d - t^2}\right] = s_g\Re\left[\frac{\frac{1}{2}\frac{h+s_d}{h-s_d}\left(t^2 + s_d\right)^2 + \left(1 - t^4\right)}{\left(t^2 - s_d\right)^2}\right] + c - 1, \tag{A9}$$

where c can be eliminated in favor of h. Depending on the signs s_d and s_g, there are four cases, each generating an equation in t and h. We proceed with each by clearing denominators and writing the expressions in the form of polynomials.

After writing relation (A9) in the variables defined in Sec. A 1 and imposing the relation (A6) we obtain the polynomial equation

$$\mathcal{P}(h, k) \equiv \left(h^2 - 1\right)\left(k^2 + 1\right)^2(k - s_d)^2 + s_g(hk - 1)\left\{h\left(k^4 + 3\right)k - 3k^4 - 1 - 2s_d\left(k^3 + k\right)(hk - 1)\right\} = 0. \tag{A10}$$

This equation must be solved along with constraints $u, v > 0$. The solution curves of different s_d and s_g are plotted in red in Fig. 21 along with the region in which both $u, v > 0$ and $\Re[\sigma] > 0$ (also written in h, k variables) in blue. Intersections of the red curve with the blue regions correspond to secondary solutions of Eq. (25) in which q is not purely imaginary.

The polynomial equation $\mathcal{P} = 0$ can be transformed into a simpler form, the Weierstraß form. Since $\mathcal{P}$ is quadratic in h we write the equation in the form $(Ah + B)^2 = m(k)^2 n(k)$ where m is quadratic or cubic in k and n is quartic in k. We then define $h' = \frac{Ah+B}{m(k)}$ so the equation takes the form $(h')^2 = n(k)$. Using standard techniques to put the curve into Weierstraß form, we choose the point $k = 1$ and compute the quadratic $\ell(k)$ that is triply tangent to $\sqrt{n(k)}$. The quantity $\ell(k)$ has a second intersection with the original curve at k_c. We define

$$l = \frac{k - 1}{h' - \ell(k)}, \qquad p = \frac{(k - 1)(k - k_c)}{h' - \ell(k)},$$

which takes the original curve to an elliptic curve in (l, p). Subsequently, we take $L = A(p)l + B(p)$ choosing A, B so that the L^2 term has unit coefficient and the term linear in L vanishes. Next take $P = Cp + D$ where C, D are chosen to set the P^3 coefficient to 4 and the P^2 coefficient to 0. The resulting elliptic curve can be parametrized by the Weierstraß $\wp$-function. After a final rescaling of both L, P to clear denominators the first case $s_d = s_g = 1$ reduces to

$$L^2 = 4P^3 - 435P + 1081,$$

whose solutions are parametrized by a particular Weierstraß $\wp$-function with elliptic invariants $(g_1, g_3) = (435, 1081)$. In fact, all four cases of different (s_d, s_g) have solution curves that can be parametrized by the *same* Weierstraß $\wp$-function albeit in different variables. We thus provide an explicit description of the solution curves.

The second condition in Eq. (A1) for the negative root can be written as

$$-\frac{8s_g s_d}{h - s_d}\Im\left[\frac{t\left(1 + ht^2\right)}{1 - t^4}\right]\Im\left[\frac{t}{s_d - t^2}\right] = s_g\Re\left[\frac{\frac{1}{2}\frac{h+s_d}{h-s_d}\left(t^2 + s_d\right)^2 - \left(1 - t^4\right)}{\left(t^2 - s_d\right)^2}\right] + c - 1 \tag{A11}$$

and reduces to another polynomial equation,

$$\mathcal{P}(k, h) \equiv \left(h^2 - 1\right)\left(k^2 + 1\right)^2(k - s_d)^2 + s_g(h - k)\left\{3hk^4 + h - \left(k^4 + 3\right)k - 2s_d\left(k^3 + k\right)(h - k)\right\} = 0. \tag{A12}$$

The solutions of this equation in each of the four cases are plotted in red in Fig. 22. This case can also be reduced to the same Weierstraß $\wp$-function.

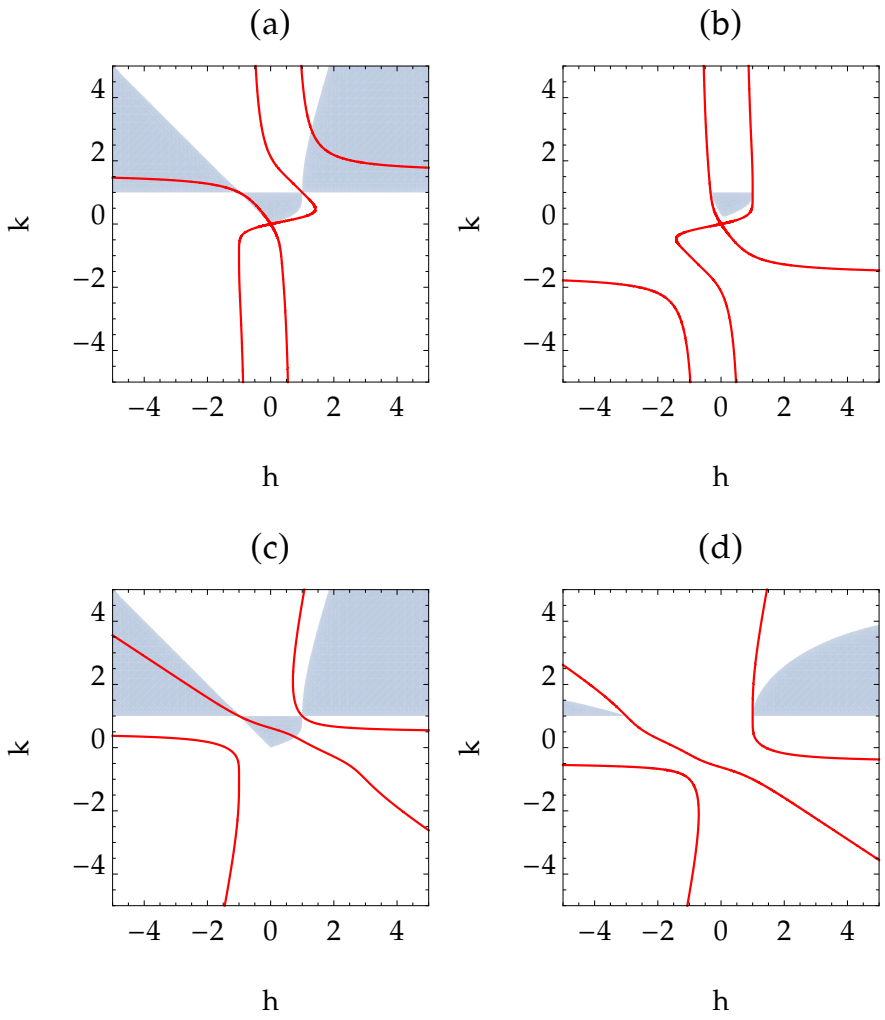

FIG. 21. Four cases of the $\Re[q] \neq 0$ generic solutions to the Benjamin-Feir stability equations for the positive root (a) $g > 0, d > 0$ (b) $g > 0, d < 0$ (c) $g < 0, d > 0$ (d) $g < 0, d < 0$. Here the zero level-set of Eq. (A10) is plotted in red and the region $u, v > 0$ and $\Im[\sigma] > 0$ is plotted in blue. The solutions correspond to the intersections of the red curve with the blue regions.

3. Velocity

The analysis above shows that there is in general either one or two solutions to the marginal stability equations for the Benjamin-Feir instability. The solution with $q_r = 0$ is given in [13] and here we show that there is also a solution $q_r \neq 0$. The secondary solution with nontrivial wave number q_r only exists under certain conditions and never coexists with the $q_r = 0$ solution. For each pair s_g, s_d the values of h for which there is instability are restricted to the following intervals:

Parameters		Instability conditions	$q_r \neq 0$	$q_r = 0$
$d > 0$	$g > 0$	$h \in (-1, 0)$	all h	nowhere
$d > 0$	$g < 0$	$h \in (-1, 1)$	$h \in \left(-1, \frac{7}{9}\right)$	$h \in \left(\frac{7}{9}, 1\right)$
$d < 0$	$g > 0$	stable		
$d < 0$	$g < 0$	$h \in (-\infty, -1) \cup (1, \infty)$	nowhere	all h

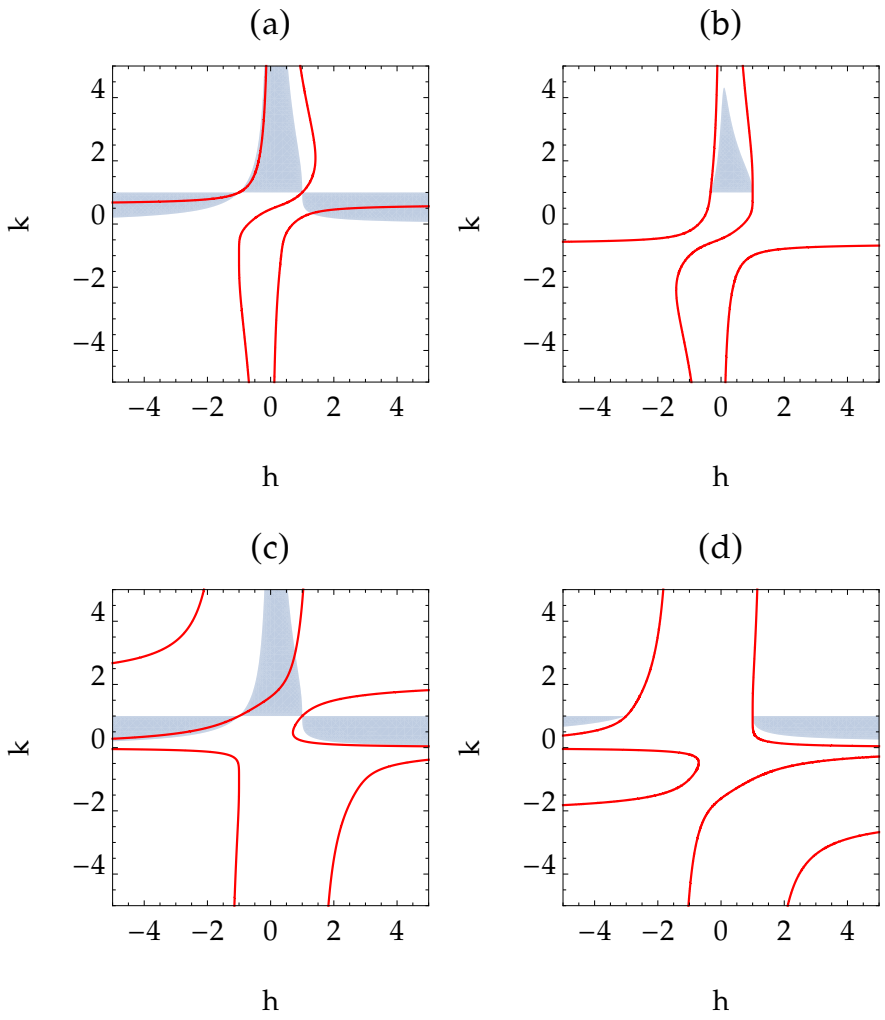

FIG. 22. Four cases of the $\Re[q] \neq 0$ generic solutions to the Benjamin-Feir stability equations for the negative root (a) $g > 0, d > 0$ (b) $g > 0, d < 0$ (c) $g < 0, d > 0$ (d) $g < 0, d < 0$. Here the zero level-set of Eq. (A10) is plotted in red and the region $u, v > 0$ and $\Im[\sigma] > 0$ is plotted in blue. The solutions correspond to the intersections of the red curve with the blue regions.

based on the instability requirements derived in [13]. The $q_r = 0$ velocity was computed in [13] but can be written in h, d variables for the two relevant cases when $g < 0$:

$$v_{BF} = \begin{cases} \frac{\left(5-\sqrt{9h^2+2h-7}-3h\right)^{\frac{3}{2}}}{\sqrt{2d}(h+1)\left(\sqrt{h+1}-\sqrt{9h-7}\right)}, & d > 0, \\ \frac{\sqrt{(h-1)(9h+7)}s_{h+1}+3h+5}{\sqrt{(h-1)(9h+7)}s_{h+1}+1-h}\sqrt{\frac{\sqrt{(h-1)(9h+7)}s_{h+1}+3h+5}{2d(1-h)}}, & d < 0. \end{cases} \tag{A13}$$

The velocity for solutions with nonzero q_r may be written

$$v_{BF} = \begin{cases} \frac{8k(s_d h-1)}{(k^2+1)(h^2-1)}\sqrt{\frac{(hk-1)(h+k)}{|d|(k^2-1)}} & (+) \\ \frac{8k(h-s_d)}{(k^2+1)(h^2-1)}\sqrt{\frac{(k-h)(hk+1)}{|d|(k^2-1)}} & (-) \end{cases}. \tag{A14}$$

The signs $(\pm)$ correspond to the two different branches of the dispersion mentioned at the beginning of this section and k is to be evaluated on the curves of solutions obtained above. Once a pair (a_1, a_2) has been selected h and d are functions of μ only, although it is typically more convenient to plot the results in terms of h. When plotted in this

fashion the h-values corresponding to $\mu = 0, \infty$ depend on a_1 and a_2.

To apply the above results we consider the instability of a rotating wave with wave number, as is observed in the wake of pulled fronts. Recall that these fronts exist along the entire line $a_1 = -a_2$ for all μ and at discrete values of μ off it. The expressions for f, g take the form

$$f = \left(4 + a_2^2 - a_1^2\right) R^4 - 2R^2$$
$$g = 2\mu + R^2,$$

where $R^2 = \frac{1}{2}\left(1 + \sqrt{4\mu + 1}\right)$ and thus $g > 0$. Based on the results above these are unstable to BF instability when $d > 0$ and the instability deposits a fixed nonzero wave number $q_r \neq 0$. With $\alpha \equiv a_2^2 - a_1^2$ the expression for c yields a relation between μ and h:

$$\mu = \frac{2(h-1)((\alpha-2)h + \alpha + 2)}{((\alpha-4)h + \alpha + 4)^2}. \tag{A15}$$

Next, d can be written in terms of h by first passing to μ variables,

$$\sqrt{|d|} = \sqrt{\left|\frac{\alpha}{4\mu+1}\right|} = \left|\frac{\alpha + (\alpha-4)h + 4}{\sqrt{\alpha}(h+1)}\right|. \tag{A16}$$

It is now clear that with this parametrization $h = \frac{2+\alpha}{2-\alpha}$ corresponds to $\mu = 0$ and $h = \frac{4+\alpha}{4-\alpha}$ to $\mu = \infty$ and $v^\dagger$, v^* and v_{BF} can all be plotted in terms of h as in Fig. 12.

Appendix B: Nonlinear selection inequalities

In this section we determine the selection pattern dictated by the inequalities (27) governing the selection of the pushed front, referred to as the nonlinear marginal stability criterion (NMS). By selection pattern we mean the intervals of $\mu \in [0, \infty)$ in which the pair of inequalities are either satisfied (N, nonlinear selection) or not (L, linear selection). The boundaries of these intervals, generically a set $\{\mu^\ddagger(a_1, a_2)\}$, occur when at least one of the inequalities becomes an equality and define the selection pattern (e.g. N–L–N or N–L...etc). In the original variables, the (a_1, a_2) dependence of the inequalities (27) is far from obvious and the expressions are manifestly unwieldy. Numerical examination of these inequalities in all three parameters is difficult to carry out, let alone visualize. To overcome this difficulty we focus only on determining possible selection patterns and not the explicit values $\{\mu^\ddagger(a_1, a_2)\}$; thus we seek general conditions on (a_1, a_2) independent of μ that are required for a given selection pattern.

To proceed we introduce changes of variables to show that (27) may be recast as a pair of quadratic inequalities. In order to determine which selection patterns are possible we reduce these to finite cases of inequalities that only depend on a_1, a_2 and not on μ. After sufficient simplification these logical statements can be verified analytically using a computer algebra system (Mathematica). We consider all possible selection patterns and show either that a particular pattern is not possible or provide a pair (a_1, a_2) for which it occurs.

We first determine which root of the Ansatz (13) is appropriate for NMS. The inequalities (27) can be rewritten as

$$\frac{\sqrt{\Gamma}}{2\sqrt{3}}\frac{\Lambda - 6}{\Delta} \pm \frac{\Gamma}{2\sqrt{3}\Delta}\sqrt{2\Lambda\left(1 + s_\Delta \frac{\mu|\Delta|}{2\Lambda}\right)} > \sqrt{\mu}, \tag{B1}$$

$$\frac{\sqrt{\Gamma}}{2\sqrt{3}}\frac{(5\Lambda - 6)}{\Delta} \pm \frac{\Upsilon}{2\sqrt{3}\Delta}\sqrt{2\Lambda\left(1 + s_\Delta \frac{\mu|\Delta|}{2\Lambda}\right)} > \sqrt{\mu}. \tag{B2}$$

Here s_Δ denotes the sign of Δ. To apply the marginal stability criterion we select the sign $(\pm)$ in the inequalities (B1) and (B2) corresponding to faster spatial decay rate and larger velocity and both must be positive at $\mu = 0$ [21]. In particular, in order for the front speed to be selected by NMS either

$$\Lambda - 6 \pm \sqrt{2\Gamma\Lambda} > 0, \qquad \sqrt{\Gamma}(5\Lambda - 6) \pm \Upsilon\sqrt{2\Lambda} > 0, \qquad \Delta > 0 \tag{B3}$$

or

$$\Lambda - 6 \pm \sqrt{2\Gamma\Lambda} < 0, \qquad \sqrt{\Gamma}(5\Lambda - 6) \pm \Upsilon\sqrt{2\Lambda} < 0, \qquad \Delta < 0 \tag{B4}$$

must hold and the root with larger velocity and faster decay rate must be chosen. When $\Delta, \Upsilon > 0$ this always corresponds to the positive root, which always exists. When $\Delta > 0$ and $\Upsilon < 0$ the positive root always exists with positive velocity while the negative root has negative velocity whenever it exists. Thus the positive root is selected. For $\Delta < 0$ and $\Upsilon > 0$ both roots violate the conditions in Eq. (B4). For $\Delta < 0$ and $\Upsilon < 0$ the positive root always satisfies the NMS conditions while the negative root never does. These results are summarized in Table I.

	$\Upsilon > 0$	$\Upsilon < 0$
$\Delta > 0$	$+$	$+$
$\Delta < 0$	NMS does not apply	$+^*$

TABLE I. The selected root of Eq. (13) for nonlinear marginal stability near $\mu = 0$. The case $\Delta, \Upsilon < 0$ is complicated at larger values of μ because the two decay rates and the corresponding velocities are oppositely ordered (see text).

It is further possible to show that when $\mu > 0$ both of the selections in the $\Delta > 0$ cases remain valid. When $\Delta < 0$ neither solution ever exists with positive velocity for $\Upsilon > 0$ while for $\Upsilon < 0$ the selection can be quite complicated. As shown in Fig. 5, for $5\Lambda - 6 < 0$ the negative sign solution exists for μ sufficiently large and this solution has positive velocity. In fact, it is easy to see from Eqs. (B1) and (B2) that when both solutions exist with positive velocity their decay rates and velocities will be oppositely ordered, $v_{N+} < v_{N-}$ and $\kappa_{N+} > \kappa_{N-}$. Because of this it is not clear that NMS applies in this μ range and which solution to choose if it does. We check whether either choice results in the selection of a nonlinear front according to the NMS inequalities.

We now proceed to reduce Eqs. (B1) and (B2) to polynomial inequalities. Because we consider $\mu > 0$ we define $\tilde{\mu} \equiv \frac{\mu|\Delta|}{2\Lambda}$ which is strictly positive and also the constants

$$b_1 = s_\Delta \frac{(\Lambda - 6)}{2\sqrt{3}} \sqrt{\frac{\Gamma}{2\Lambda|\Delta|}}, \qquad b_2 = s_\Delta \frac{\Gamma}{2\sqrt{3|\Delta|}}, \qquad b_3 = s_\Delta \frac{(5\Lambda - 6)}{2\sqrt{3}} \sqrt{\frac{\Gamma}{2\Lambda|\Delta|}}, \qquad b_4 = s_\Delta \frac{\Upsilon}{2\sqrt{3|\Delta|}} \tag{B5}$$

so that the pair of inequalities take the form $b_i \pm b_{i+1}\sqrt{1 + s_\Delta \tilde{\mu}} > \sqrt{\tilde{\mu}}$ for $i = 1, 2$. To eliminate the square roots we introduce a holomorphic substitution $\tilde{\mu} = f(t)$ with $t \in (0, 1)$ (see Table B) chosen to be bijective on the full domain $\tilde{\mu} \in [0, \infty)$ so that the arguments of both roots are squares of positive quantities. After this substitution each inequality reduces to an inequality quadratic in the parameter t.

s_Δ	$\tilde{\mu}$	$1 + s_\Delta \tilde{\mu}$	$\tilde{\mu}$−domain	$b_i \pm b_j\sqrt{1 + s_\Delta \tilde{\mu}} > \sqrt{\tilde{\mu}}$
1	$\frac{4t^2}{(1-t^2)^2}$	$\frac{(1+t^2)^2}{(1-t^2)^2}$	$\tilde{\mu} \in (0, \infty)$	$(b_j - b_i)t^2 - 2t + (b_i + b_j) > 0$
-1	$\frac{4t^2}{(1+t^2)^2}$	$\frac{(1-t^2)^2}{(1+t^2)^2}$	$\tilde{\mu} \in (0, 1)$	$(b_i \mp b_j)t^2 - 2t + (b_i \pm b_j) > 0$

TABLE II. Substitutions that eliminate both square roots in Eqs. (B1) and (B2). The root signs have been chosen to match s_Δ according to the relevant roots classified in Table I. In both cases $t \in (0, 1)$.

At this point the question of selection can be reduced to one of solving quadratic equations in t in the interval $(0, 1)$. In the generic case, each of the inequalities Eqs. (B1) and (B2) lose validity at μ values for which an inequality becomes an equality, or the square root of the quadratic terms in Table B becomes zero. That is, the intervals on which the selection is either N or L are separated by points at which at least one of the inequalities becomes an equality. The nongeneric case in which a double root occurs is of higher codimension and is dealt with separately. Thus we can determine selection patterns by tracking the roots obtained when Eq. (B1) and Eq. (B2) are *equalities*. Each of Eq. (B1) and Eq. (B2) corresponds to a single quadratic equation which may have 0, 1, or 2 roots in $(0, 1)$, so there are 19 possible arrangements of the roots each of which could be a different selection pattern. In what follows we show that the only possible selection regimes are N, L, and N–L. Thus the set $\{\mu^\ddagger(a_1, a_2)\}$ reduces to a single member where $\mu^\ddagger(a_1, a_2)$ is either 0 (L), finite (N–L) or ∞ (N).

To proceed we derive t-independent conditions on the coefficients of the quadratic equations that determine properties of their roots. We organize this discussion based on various properties of the root arrangements. To simplify the discussion we introduce two polynomials

$$\begin{aligned} h_1(t) &= \alpha t^2 - 2t + \beta, \\ h_2(t) &= \gamma t^2 - 2t + \delta \end{aligned} \tag{B6}$$

to represent the two polynomials inherited from Eqs. (B1) and (B2). We assume $\beta > 0$ based on the qualification in [21] that NMS holds when the nonlinear velocity is positive at $\mu = 0$. Without loss of generality we also assume that Eq. (B2) is satisfied at $m = 0$ because it is proportional to a_N^2 so $\delta > 0$. We use the standard logical notation for "AND", $A \wedge B$ to represent the condition that A and B are both true. Note that since the conditions generally depend on parameters, the joint condition $\wedge_i A_i$ is only false when it fails for *all* parameter values. Recall that both Γ, Λ are positive and the conditions $(\Gamma > 0) \wedge (\Upsilon > 0) \wedge (5\Lambda - 6 < 0)$ and $(\Gamma > 0) \wedge (\Upsilon < 0) \wedge (\Lambda - 6 > 0)$ are false.

1. Number of roots

In subcritical systems Eq. (27) is typically satisfied at $\mu = 0$, so if both equations (B6) have an even number of roots the inequalities will also be satisfied for $\mu \to \infty$. This is unphysical since at a sufficiently large forcing the linear dynamics usually take over [21]. In order to translate this property to one of the quadratic roots consider h_1. If $h_1(0) > 0$ then the equation has an even number of roots in $(0, 1)$ provided $h_1(1) > 0$ (recall that we exclude the nongeneric case of double roots) or

$$\beta > 0 \quad \text{and} \quad \alpha - 2 + \beta > 0$$

with a similar statement for h_2. In order to distinguish between the polynomial having zero or two roots we also check the discriminant and the derivative at $t = 1$. If the polynomial has positive discriminant then it has two roots. If there are two roots, because both polynomials have derivative -2 at $t = 0$ then both roots are in $(0, 1)$ if and only if the derivative is positive at $t = 1$. These conditions (for two roots) are

$$\alpha\beta < 1 \quad \text{and} \quad \alpha > 1. \tag{B7}$$

Applying this procedure to the equations from Table B yields the conditions in Table B 1.

s_Δ	even # of roots	2 roots
1	$b_j > 1$ and $b_i > -b_j$	$b_j^2 - b_i^2 < 1$ and $b_j - b_i > 1$
-1	$b_i > 1$ and $b_i > -b_j$	$b_i^2 - b_j^2 < 1$ and $b_i - b_j > 1$

TABLE III. Conditions for each of Eqs. (B1) and (B2) to have an even number of points of equality. In the case $\Delta < 0$ the positive root was selected.

a. *Case* Δ, $\Upsilon > 0$

The conditions for an even number of roots are:

$$\left(\Gamma^2 > 12|\Delta|\right) \wedge \left(\Lambda - 6 > -\sqrt{2\Lambda\Gamma}\right), \qquad \left(\Upsilon^2 > 12|\Delta|\right) \wedge \left((5\Lambda - 6)\sqrt{\Gamma} > -\Upsilon\sqrt{2\Lambda}\right) \tag{B8}$$

which can be true individually or both together. The conditions for two roots are:

$$\left(2\Lambda\Gamma^2 - (\Lambda - 6)^2\Gamma < 24\Delta\Lambda\right) \wedge \left(2\sqrt{3}\sqrt{2\Lambda\Delta} < \Gamma\sqrt{2\Lambda} - (\lambda - 6)\sqrt{\Gamma}\right), \tag{B9}$$

$$\left(2\Lambda\Upsilon^2 - (5\Lambda - 6)^2\Gamma < 24\Delta\Lambda\right) \wedge \left(2\sqrt{3}\sqrt{2\Lambda\Delta} < \Upsilon\sqrt{2\Lambda} - (5\lambda - 6)\sqrt{\Gamma}\right). \tag{B10}$$

The first of these Eq. (B9) can be true or false but Eq. (B10) is false for all parameters so h_1 always has 0 or 1 roots. A summary of all possible scenarios is provided in Table IV along with sample parameters when possible. These results rule out 12 of the possible 19 root arrangements.

b. *Case* $\Delta > 0$, $\Upsilon < 0$

The conditions for an even number of roots of h_1 are the same as those above but must now be checked along with $\Upsilon < 0$ instead. For h_2 it is easy to see that the condition $b_j > 1$ or $\Upsilon > 2\sqrt{3\Delta}$ fails and it therefore always has a

		$h_1(t)$		
		zero	one	two
$h_2(t)$	zero	$(-15, 16)$	$\left(3, \frac{9}{2}\right)$	impossible
	one	impossible	$(2, 2)$	$\left(0, \frac{1}{2}\right)$
	two	impossible	impossible	impossible

TABLE IV. Summary of the possible numbers of roots for $\Delta,\ \Upsilon > 0$. When the condition can be satisfied an example (a_1, a_2) for which this is possible is shown. All of the parameters except the zero-zero case satisfy the known condition sufficient for global existence of solutions to the Cauchy problem.

		$h_1(t)$		
		zero	one	two
$h_2(t)$	zero	impossible	impossible	impossible
	one	impossible	$\left(2, \frac{1}{5}\right)$	$\left(-\frac{7}{4}, 0\right)$
	two	impossible	impossible	impossible

TABLE V. Summary of the possible numbers of roots for $\Delta > 0,\ \Upsilon < 0$. When the condition can be satisfied an example (a_1, a_2) for which this is possible is shown. All of the parameters satisfy the known condition sufficient for global existence of solutions to the Cauchy problem.

single root. As before the allowed possibilities are summarized in Table V and a total of 14 root configurations are ruled out.

c. *Case* $\Delta < 0,\ \Upsilon < 0$

In this section we only treat the positive root of Eqs. (B1) and (B2) and leave the case where both roots exist to Sec.B 4. The conditions for an even number of roots are

$$\left((\Lambda-6)^2\Gamma > 24\Lambda|\Delta|\right) \wedge \left((\Lambda-6)^2\Gamma > 2\Lambda\Gamma\right), \qquad \left(-(5\Lambda-6)\sqrt{\Gamma} > 2\sqrt{3}\sqrt{2\Lambda|\Delta|}\right) \wedge \left(-(5\Lambda-6)\sqrt{\Gamma} > \Upsilon\sqrt{2\Lambda}\right), \tag{B11}$$

where we used the fact that $\Lambda - 6$ is negative in this regime to simplify the expressions. The latter set of inequalities is always false so h_2 always has a single root. The condition for two roots of h_1 is

$$\left((\Lambda-6)^2\Gamma - 2\Lambda\Gamma^2 < 24\Lambda|\Delta|\right) \wedge \left(-(\Lambda-6)\sqrt{\Gamma} + \Gamma\sqrt{2\Lambda} > 2\sqrt{3}\sqrt{2\Lambda|\Delta|}\right). \tag{B12}$$

Checking the three remaining cases produces the results in Table VI.

2. Root ordering

Next we derive conditions to determine the root ordering for the two polynomials. This dictates whether or not the selected velocity can jump discontinuously.

If selection of either L or N changes three times there will generically be a discontinuous jump in the selected velocity. The analysis in Sec. B 1 does not rule this out because in the case that h_1 has two roots and h_2 has one,

		$h_1(t)$		
		zero	one	two
$h_2(t)$	zero	impossible	impossible	impossible
	one	impossible	$\left(-2, \frac{1}{2}\right)$	$(-2, 1)$
	two	impossible	impossible	impossible

TABLE VI. Summary of the possible numbers of roots for $\Delta < 0,\ \Upsilon < 0$. When the condition can be satisfied an example (a_1, a_2) for which this is possible is shown. None of the regimes fall in the known global existence region.

both roots of h_1 may be smaller than that of h_2. Thus when the root of h_2 is encountered (as μ is increased) the predicted velocity will jump discontinuously. We assume that h_2 has a single root in the interval because the case in which both quadratics have two roots in $(0,1)$ was ruled out in Sec. B 1. Another possible cause of discontinuity in the selected velocity occurs if Eq. (B2) breaks first, before Eq. (B1), since both inequalities are satisfied at $\mu = 0$. Given the previous results this can only occur in the case that h_2 has one root in $(0,1)$ that is smaller than any of the roots of h_2 in the interval.

We now derive a condition that is implied by the two root orderings mentioned above, thus indicating whether or not they can occur. First, it is possible to show that $\delta > \beta > 0$ regardless of the parameter values. Because of this ordering it is clear that for either of the two properties mentioned above to occur, h_1 and h_2 must cross *and* the common value must be positive. In the former case t_{cross} is greater than both roots of h_1, and in the latter case t_{cross} is smaller than any roots of either polynomial. It is easy to see that the difference of the polynomials, $(h_2 - h_1)(t) = (\gamma - \alpha)t^2 + (\delta - \beta)$ has either zero roots or two roots of opposite signs. Since $h_2(0) > h_1(0)$ then the root of h_2 is smaller than those of h_1 if and only if $h_2 - h_1$ has a root $t_{cross} \in (0,1)$ such that $(h_2 - h_1)(t_{cross}) > 0$. These conditions are equivalent to the conditions

$$\begin{aligned} \gamma + \delta < 2 \qquad & h_2 \text{ has one root in } (0,1) \\ \gamma - \alpha < 0 \qquad & h_2 - h_1 \text{ has a root} \\ \delta - \beta < \gamma - \alpha \qquad & t_{cross} \in (0,1) \\ (\gamma - \alpha)(\delta - \beta) + \delta - \beta > 0 \qquad & (h_2 - h_1)(t_{cross}) > 0. \end{aligned}$$

We have verified that these conditions cannot be satisfied which shows that the selected velocity cannot suffer discontinuous jumps.

3. The case of double roots

Each double root in either of the quadratic inequalities generically drops the dimension of phase space by one. In order for a double root to exist the discriminant must vanish, either $\alpha\beta = 1$ or $\gamma\delta = 1$. In each case these conditions factor,

$$(a_1 + a_2)\Delta = 0, \tag{B13}$$
$$\left(16 + (a_1 + a_2)(3a_1 + 11a_2)\right)\Delta = 0, \tag{B14}$$

and each case can be reduced to a 1-parameter space of solutions. It can be shown that $16 + (a_1 + a_2)(3a_1 + 11a_2) = 0$ is incompatible with the requirement $\Gamma > 0$, so the second case can be reduced further to $\Delta = 0$. Interestingly, if there are two double roots the solutions are still described by a 1-parameter space, parametrized exactly by $\Delta = 0$. As mentioned in II B, when $\Delta = 0$ the Ansatz solutions that are used here cease to be valid and a different analysis has to be conducted using the appropriate solutions. We omit this step.

Excluding the case $\Delta = 0$ we analyze the root structure for a single double root of h_1. When $a_1 = -a_2$ then h_1 has a double root and all of the coefficients collapse to $h_1(t) = \sqrt{3}\left(t - \frac{1}{\sqrt{3}}\right)^2$, $h_2(t) = -2\left(t - \frac{1}{\sqrt{3}}\right)$. The roots are independent of parameters and coincide. This is the classic case that arises when $a_1 = a_2 = 0$ and hereby extends along the whole line $a_1 + a_2 = 0$.

4. The case Υ, $\Delta < 0$ with both solutions of the Ansatz

In this case the negative root solution to Eq. (13) exists for $\mu \in \left(1 - \frac{\Gamma(5\Lambda-6)^2)}{2\Lambda\Upsilon^2}, 1\right]$ and corresponds to a positive velocity. Although this solution does not exist at $\mu = 0$, this velocity can be compared to the linear prediction. Because we know that $\kappa_{N+} > \kappa_{N-}$ and $\kappa_{N-} = 0$ at $\mu = 1 - \frac{\Gamma(5\Lambda-6)^2)}{2\Lambda\Upsilon^2}$ we focus on h_2 in order to see if Eq. (B2) can ever be satisfied. First one can check that $\gamma + \delta < 2$, which means that h_2 is negative at 1. Since we know that h_2 is negative at $\mu = 1 - \frac{\Gamma(5\Lambda-6)^2)}{2\Lambda\Upsilon^2}$ this means that it has either 0 or two roots. Then one can check that $\gamma\delta < 1$ (h_2 has roots) and $\gamma < 0$ (h_2 is positive between the roots) cannot both be satisfied. Thus the a_{N-} branch is never relevant.

Appendix C: Numerical methods

Time-stepping simulations were carried out using two numerical approximation schemes. The first is a Fourier collocation method with suitable de-aliasing and the time-stepping scheme ETD4RK [41]. Depending on the

initial data and the possible types of front propagation behavior the simulations are either performed in a frame at rest or in one moving at constant speed. In the moving frame the spatially extended front solutions typically have a nontrivial wave number $q_N \neq 0$ in the limit $\xi \to -\infty$. To overcome the difficulty of approximating the boundary condition for this state, we write $A(x,t) = \tilde{A}(\xi,t)e^{i(q_N\xi-\omega t)} = \tilde{A}(\xi,t)e^{iq_N x}$ and solve the following equation instead:

$$\tilde{A}_t = (\mu - q_N^2)\tilde{A} + (v + 2iq_N)\tilde{A}_\xi + \tilde{A}_{\xi\xi} + i\left(a_1|\tilde{A}|^2\tilde{A}_\xi + a_2\tilde{A}^2\bar{\tilde{A}}_\xi\right) + \left(1 + q_N(a_2 - a_1) - |\tilde{A}|^2\right)|\tilde{A}|^2\tilde{A} \tag{C1}$$

subject to Neumann (Dirichlet) conditions on the real (imaginary) part of the solution at both boundaries. After an initial de-aliasing Heaviside initial conditions generate continuous initial data.

We also employ a finite difference (FD) method using implicit Euler for the time discretization. The FD simulation is carried out in the stationary frame with Dirichlet boundary conditions imposed on both real and imaginary parts of the solution. We study the evolution of localized Heaviside initial data originating in the center of the domain. The scheme takes the form

$$\frac{u_i^{j+1} - u_i^j}{\Delta t} = \mathcal{L}\left(u_{i-1}^{j+1}, u_i^{j+1}, u_{i+1}^{j+1}\right) + \mathcal{N}\left(u_{i-1}^{j}, u_i^{j}, u_{i+1}^{j}\right), \tag{C2}$$

where u_i^j is the solution value at spatial point i and time step j and centered differences are used for all of the spatial derivatives. The operators $\mathcal{L}$ and $\mathcal{N}$ indicate the linear and nonlinear terms in the evolution equation, respectively.

When $\mu > 0$ the $A = 0$ state is unstable resulting in the amplification of any numerical instabilities that occur ahead of the front. Growth of such instabilities interferes with the propagation of the leading edge and renders a velocity measurement of the initial leading edge impossible. For the FD code this is not a problem since solution values initialized at 0 remain 0 until the leading edge reaches them. However, the Fourier scheme propagates small errors in each mode throughout the spatial domain and can nucleate instabilities ahead of the front. To prevent this we set $A(x) = 0$ for any x such that $|A(x)| < \epsilon$ at every time step. If ϵ is small enough this has the effect of quenching instabilities ahead of the front before they can grow but leaves the front at amplitude above ϵ intact. The required magnitude of ϵ depends on both the time-step and the value of μ and is chosen to be as large as feasible. Values of ϵ used here vary from 10^{-12} to $10^{-4.5}$. For any $\epsilon > 0$, but decreasingly as it is reduced, the cutoff affects the speed of the front. Because it quenches the instability of the leading state the speed of pulled fronts is reduced. This makes any prediction of the front velocity difficult and typically produces a speed less than the analytical prediction. Consequently we almost exclusively use the FD method to explicitly measure front speeds.

In order to measure the velocity of fronts numerically we select a fixed height h and calculate the trajectory, x_f, of the level set $|A(x_f)| = h$. After an initial transient the front reaches a constant velocity and we measure its speed $\dot{x_f}$ by a linear fit to $x_f(t)$. We keep h as small as possible to avoid behavior that occurs behind the leading edge. The prescription for computing the data in Figs. 10 and 11 is:

- Initialize Heaviside initial data of extent 50 at the center of the domain of length 300. Run a simulation with $\Delta x = 0.05$ and $\Delta t = (\Delta x)^2$.
- The simulation is run for time $T = \frac{100}{2\sqrt{v^*\Delta t}}$ and the location of the front is measured by the level set with $h = 0.01$. This allows the front to remain a distance > 50 away from the boundary throughout the experiment. For simulations near $\mu = 0$, where $v^* = 0$, the simulation time is taken to be in the range $[30000, 50000]$ such that a stable velocity is achieved and $h = 0.0001$.
- A line is fitted to the second half of the data $x_f(t)$ (i.e. $t > \frac{T}{2}$) to measure the front speed. This ensures that we discard the transient associated with the initial condition and measure the front speed only for a well-developed front.

It is pointed out in [42] that for an FD scheme an exact prediction of the errors in the linear spreading speed in terms of the FD discretization can be derived. Letting $u_m^n = \epsilon e^{\sigma_{FD}(n\Delta t) - iq_{FD}(m\Delta x)}$ in (C2) and keeping lowest order terms in ϵ yields the FD dispersion relation $\sigma_{FD}(q_{FD})$ which solves the transcendental equation

$$\frac{1 - e^{-\sigma_{FD}\Delta t}}{\Delta t} = \mu - \left(\frac{2}{\Delta x}\sin\left(\frac{\Delta x q_{FD}}{2}\right)\right)^2. \tag{C3}$$

In the limit $\Delta x, \Delta t \ll 1$ we can apply the marginal stability criterion and determine that

$$
\begin{aligned}
v^*_{FD} &= 2\sqrt{\mu} + 2\mu^{\frac{3}{2}}(\Delta t) + \frac{5\mu^{\frac{5}{2}}}{3}(\Delta t)^2 + \frac{\mu^{\frac{3}{2}}}{12}(\Delta x)^2 + \mathcal{O}(\Delta t, \Delta x)^3\,, \\
q^*_{FD} &= i\left[\sqrt{\mu} - \mu^{\frac{3}{2}}(\Delta t) + \frac{5\mu^{5/2}}{6}(\Delta t)^2 - \frac{\mu^{3/2}}{8}(\Delta x)^2\right] + \mathcal{O}(\Delta t, \Delta x)^3\,, \\
\sigma^*_{FD} &= 2\mu + \frac{4\mu^3}{3}(\Delta t)^2 - \frac{\mu^2}{6}(\Delta x)^2 + \mathcal{O}(\Delta t, \Delta x)^3
\end{aligned}
\tag{C4}
$$

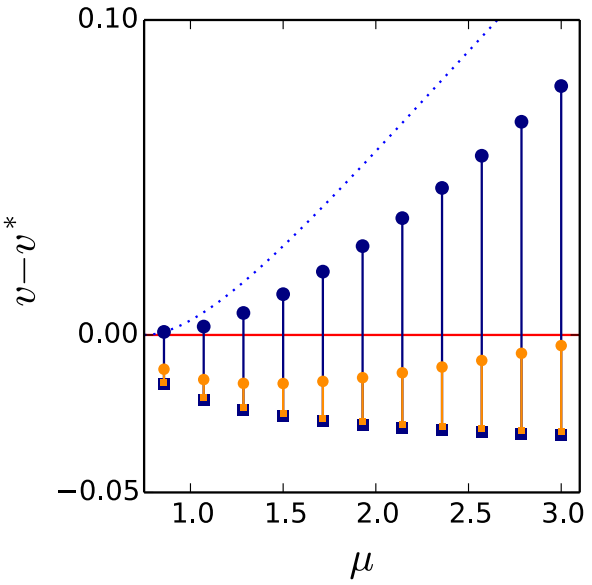

FIG. 23. Front speed v_N (blue) relative to the linear spreading speed v^* (red) for parameters $(a_1, a_2) = (0, 0)$. The selected (not selected) speed is indicated by a solid (dashed) line according to Eq. (27). The navy ($\Delta x = 0.1$) and orange ($\Delta x = 0.05$) circles represent speeds calculated by time-stepping Heaviside initial conditions using FD in the stationary frame and tracking the motion of the front with $\Delta t = (\Delta x)^2$. The squares represent the values of the speeds after subtracting the corrections identified in Eq. (C4).

by solving linear algebraic problems order by order. Since Δx, Δt are assumed to be positive, the signs of the resulting corrections are determined. Here we assume that the errors do not cause the spreading wave number to become complex. We have not seen any evidence in our numerics that this should be the case and it greatly simplifies the calculation. Because the time integration uses a first order method the resulting velocity has an error of first order in Δt. However, since we impose the constraint that $\Delta t = (\Delta x)^2$ in every simulation so the error is $\mathcal{O}((\Delta x)^2)$.

Assuming that the method for measuring the velocity from simulations is accurate and a pulled front occurs, then the measured front velocity is biased deterministically by the corrections in Eq. (C4). We can interpret the analytically predicted corrections in two ways. We can either compare simulation results directly to v^*_{FD} and not v^* or we can subtract the deterministic correction $v^*_{FD} - v^*$ from the data and compare it to v^*. In this work we have chosen to plot the simulation data with an error bar showing the unbiased quantity because we do not have any result concerning the corrections to v_N due to FD (Figs. 10 and 11). The corrected value effectively *eliminates the discretization error* caused by the finite differences approximation but does not mitigate any other errors that could be introduced by the simulation parameters or implementation. A comparison of these corrections for simulations with varying discretizations Δx is shown in Fig. 23. Here the measured data are shown as circles and the corrected data as squares. The collapse of the data after corrections have been subtracted supports the robustness of the corrections in Eq. (C4) and suggests that there is an additional slowing of the velocity below the expected v^* value. This slowing is almost certainly due to the imposed Dirichlet boundary conditions in the simulation which artificially pin the leading edge of the front. The effect of boundary conditions and finite domain size is studied in [42] and is known to lead to this type of slowing down.

[1] M. C. Cross and P. C. Hohenberg, Rev. Mod. Phys. **65**, 851 (1993).
[2] S. Tobias, M. Proctor, and E. Knobloch, Physica D **113**, 43 (1998).
[3] A. Hari and A. A. Nepomnyashchy, Phys. Rev. E **61**, 4835 (2000).
[4] W. van Saarloos, Phys. Rep. **386**, 29 (2003).
[5] A. J. Archer, M. C. Walters, U. Thiele, and E. Knobloch, Phys. Rev. E **90**, 042404 (2014).
[6] W. Eckhaus and G. Iooss, Physica D **39**, 124 (1989).
[7] A. Doelman and W. Eckhaus, Physica D **53**, 249 (1991).
[8] J. Duan and P. Holmes, Proc. Edinburgh Math. Soc. **38**, 77 (1995).
[9] T. Kapitula, Comm. Pure Appl. Math. **47**, 831 (1994).
[10] T. Kapitula, Physica D **82**, 36 (1995).
[11] A. Shepeleva, Nonlinearity **11**, 409 (1998).
[12] H.-C. Kao and E. Knobloch, Phys. Rev. E **85**, 026211 (2012).

[13] H.-C. Kao and E. Knobloch, Math. Model. Nat. Phenom. **8**, 131 (2013).
[14] J. Duan and P. Holmes, Nonlinear Anal. Theor. **22**, 1033 (1994).
[15] J. Duan, P. Holmes, and E. S. Titi, Nonlinearity **5**, 1303 (1992).
[16] W. van Saarloos, Phys. Rev. A **39**, 6367 (1989).
[17] H. Tian, Z. Li, J. Tian, and G. Zhou, Phys. Rev. E **66**, 066204 (2002).
[18] G. Dee and J. S. Langer, Phys. Rev. Lett. **50**, 383 (1983).
[19] W. van Saarloos, Phys. Rev. A **37**, 211 (1988).
[20] W. van Saarloos and P. C. Hohenberg, Phys. Rev. Lett. **64**, 749 (1990).
[21] W. van Saarloos and P. C. Hohenberg, Physica D **56**, 303 (1992).
[22] K. Nozaki and N. Bekki, J. Phys. Soc. Jpn. **53**, 1581 (1984).
[23] A. Couairon and J.-M. Chomaz, Physica D **108**, 236 (1997).
[24] L. N. Trefethen and M. Embree, *Spectra and Pseudospectra: The Behavior of Nonnormal Matrices and Operators* (Princeton University Press, 2005).
[25] J.-M. Chomaz, Annu. Rev. Fluid Mech. **37**, 357 (2005).
[26] P. J. Schmid, Annu. Rev. Fluid Mech. **39**, 129 (2007).
[27] J. M. Dixon, J. A. Tuszynski, and P. A. Clarkson, *From Nonlinearity to Coherence: Universal Features of Nonlinear Behaviour in Many-Body Physics* (Clarendon, Oxford, 1997).
[28] D. G. Aronson and H. F. Weinberger, in *Partial Differential Equations and Related Topics*, edited by J. A. Goldstein (Springer Berlin Heidelberg, Berlin, Heidelberg, 1975) pp. 5–49.
[29] D. Aronson and H. Weinberger, Adv. Math. **30**, 33 (1978).
[30] E. M. Lifshitz and L. P. Pitaevskii, *Physical Kinetics, Course of Theoretical Physics*, Vol. 10 (Pergamon, New York, 1981).
[31] L. Brevdo and T. J. Bridges, Phil. Trans. R. Soc. A **354**, 1027 (1996).
[32] P. Huerre and P. A. Monkewitz, J. Fluid Mech. **159**, 151 (1985).
[33] P. Huerre and P. A. Monkewitz, Annu. Rev. Fluid Mech. **22**, 473 (1990).
[34] A. Bers, in *Basic Plasma Physics: Selected Chapters, Handbook of Plasma Physics, Volume 1*, edited by A. A. Galeev and R. N. Sudan (1984) p. 451.
[35] J. A. Sherratt, A. S. Dagbovie, and F. M. Hilker, Bull. Math. Biol. **76**, 1 (2014).
[36] E. Ben-Jacob, H. Brand, G. Dee, L. Kramer, and J. Langer, Physica D **14**, 348 (1985).
[37] J. A. Powell, A. C. Newell, and C. K. R. T. Jones, Phys. Rev. A **44**, 3636 (1991).
[38] R. D. Benguria and M. C. Depassier, Phys. Rev. Lett. **73**, 2272 (1994).
[39] R. D. Benguria and M. C. Depassier, Commun. Math. Phys. **175**, 221 (1996).
[40] K. Nozaki and N. Bekki, Phys. Rev. Lett. **51**, 2171 (1983).
[41] S. M. Cox and P. C. Matthews, J. Comput. Phys. **176**, 430 (2002).
[42] U. Ebert and W. van Saarloos, Physica D **146**, 1 (2000).